THE EFFECT OF PHASE FRACTIONS AND MANGANESE CONTENT ON THE CORROSION PROPERTIES OF QUENCHED AND PARTITIONED MARTENSITIC STAINLESS STEEL

A thesis submitted to the Delft University of Technology in fulfillment
of the requirements for the degree of:

Master of Science in Materials Science and Engineering

December 9, 2021

by

Leon Crousen
(4741714)

Supervisor: Dr Yaiza Gonalez-Garcia
Thesis Committee: Prof. Maria Santofimia
Dr. Dessi Koleva
Gaojie Li

”All we have to decide is what to do with the time that is given us.”

J.R.R. Tolkien
The Fellowship of The Ring

ABSTRACT

A long standing research field in material science has been the trade-off between strength and ductility of steels. Advanced High Strength Steels (AHSS) aim to combine these two properties and provide steels that can increase safety and lower CO_2 consumption in automotive applications, by decreasing weight. To further decrease the environmental impact, novel quenched and partioned (Q&P) martensitic stainless steel is considered to prevent corrosion. Quenching and partitioning is a heat treatment that aims for a martensite/retained austenite microstructure with specific phase fractions to optimize strength and ductility. While mechanical properties are well researched for Q&P treated martensitic stainless steel, the corrosion properties are not that widely documented.

This thesis aims to discover the influence of the microstructural development in terms of phase fractions due to the Q&P treatment, and the manganese content on the corrosion properties of martensitic stainless steel. Two alloys with chemical composition 0.2C-12.5Cr-0.35Si-XMn, where X stands for 0.7 for the low manganese alloy, and 3 for high manganese alloy, are considered for this study, and are compared to a commercial AISI 420 martensitic stainless steel. The microstructure was investigated by the use of optical microscopy, energy dispersive X-ray spectroscopy (EDS), electron probe microanalysis (EPMA), scanning Kelvin probe force microscopy (SKPFM). This was combined with electrochemical experiments including Open-circuit potential measurements, potentiodynamic polarization and electrochemical impedance spectroscopy (EIS).

When compared to commercially available AISI 420 martensitic stainless steel, the novel Q&P MSS showed improved corrosion properties. This can mainly be attributed to the lack of chromium rich carbides ($Cr_{23}C_6$ or Cr_7C_3) in the Q&P treated MSS. However, this improvement in corrosion properties was only observed for the samples with low manganese content.

The increase of fraction retained austenite did show an increase in corrosion potential, making the steel more cathodic, but the improvements in terms of pitting potential and passive film properties are limited. Samples with high fresh martensite fractions also showed an increase in corrosion potential, but only marginally increased in terms of length of the passive region. EIS data shows that the addition of fresh martensite reduces the passivity properties of the material. Volta-potential measurements done by SKPFM showed a clear difference between primary martensite and fresh martensite of up to 20mV and were overlapping with the topography maps. This can be an indication of increased tendency to form micro-galvanic cells between martensite phases.

Manganese was found to be detrimental for the corrosion properties of the Q&P treated MSS. A clear drop in the length of the passive region shows that the high manganese samples are more susceptible to pitting. EDS measurements and EPMA elemental distribution maps showed local zones of decreased chromium and increased manganese and silicon. This indicates that there are secondary phase particles present in the material in the form of manganese silicide or manganese sulfide. Volta-potential measurements done by SKPFM showed these particles behave more anodic in comparison to the matrix of the material. The number of particles per unit area was increased for the samples with high manganese content. These inclusions greatly reduce corrosion performance, showing that the addition of manganese is detrimental for corrosion performance.

Several other microstructural features are discussed in terms of influence on the corrosion performance of the material. Which include prior austenite grain boundaries, elemental banding of chromium and manganese and Volta-potential differences between martensite laths.

ACKNOWLEDGEMENTS

This thesis marks the end of my masters program. While much of my second master-year was during the COVID-19 times, I still very much enjoyed my studies.

Firstly, I would like to thank my supervisor Dr. Yaiza Gonzalez-Garcia. You were always approachable for questions, and showed me that careful data evaluation can often be more important than repeating experiments. Beside this, you greatly helped me in the last year of my Master's program, be it by inspiring lecture or supervising my project.

I also whish to thank Gaojie Li and Dr. Aytac Yilmaz. Both of you helped me with either microstructure characterization, or learning difficult techniques like SKPFM. For help with microstructural characterization using EPMA and EDS i would like to thank Kees Kwakernaak

Last, but not least, my appreciation goes out to all my friends and family. You often believed more in me than I did in myself.

CONTENTS

LIST OF FIGURES

LIST OF TABLES

ACRONYMS

AHSS	Advanced High Strength Steels
MSS	Martensitic Stainless Steel
TRIP	Transformation Induced Plasticity
Q&P	Quenching and Partitioning
Q&T	Quenching and Tempering
M_s	Martensite Start Temperature
M_f	Martensite Finish Temperature
CPE	Constrained Para-Equilibrium
CCE	Constrained Carbon Equilibrium
SKPFM	Scanning Kelvin Probe Force Microscopy
AFM	Atomic Force Microscopy
EPMA	Electron Probe Microanalysis
EDS	Energy Dispersive X-Ray Spectroscopy
EIS	Electrochemical Impedance Spectroscopy
OCP	Open Circuit Potential

1 INTRODUCTION

A classic research field in the development of steel is the relation between ductility and strength. Steels consisting of ductile phases like ferrite often lack the mechanical properties (strength) to be used in specific applications. On the other hand, steels dominated by strong and hard phases like martensite often lack ductility, limiting their applications. The automotive industry is constantly improving the safety and fuel efficiency of cars. One major aspect of development is the Advanced High Strength Steel (AHSS). These are steels with multiphase microstructures like dual-phase steels, complex phase steels, TRIP steels and martensitic steels [5]. These AHSS combine the unique combination of high strength and good ductility by combining the hard phases like martensite or bainite with softer phases like ferrite and austenite [6].

One development in this field is the research in microstructures consisting of martensite and retained austenite. This combination of phases provides the strength and ductility needed. The martensite provides a certain strength to the material, and the retained austenite provides a certain measure of ductility which, under strain, will undergo a phase transformation to martensite. While TRIP steels are widely researched and processed according to well-known thermo-mechanical treatments, there are other methods to achieve the desired retained austenite in a martensite matrix that can provide stronger and more ductile steel by controlling the different fractions with higher accuracy[1; 7]. Quenching and partitioning have been proposed and widely applied for the development of AHHS [8; 2]. This heat treatment has been demonstrated to yield a good combination of high strength and high ductility. This treatment is based on the fact that carbon can diffuse from supersaturated martensite to untransformed austenite. This added carbon stabilizes the austenite at room temperature. Hence, the name retained austenite. The process will be explained in more detail in Chapter 2 of this thesis.

Quenched and partitioned steels are known as third-generation AHSS. They provided a significant increase in the combination of strength and ductility over the first-generation AHSS, like dual-phase or TRIP steel. Second-generation AHSS, like TWIP (twinning-induced plasticity) steel, still provide overall a better performance in terms of strength and ductility. However, these steels often form processing challenges, and are very expensive due to the high alloying content required to reach the austenitic structure. The third-generation AHSS aims to bridge this gap and provide sufficient strength and ductility, while still being economically viable.

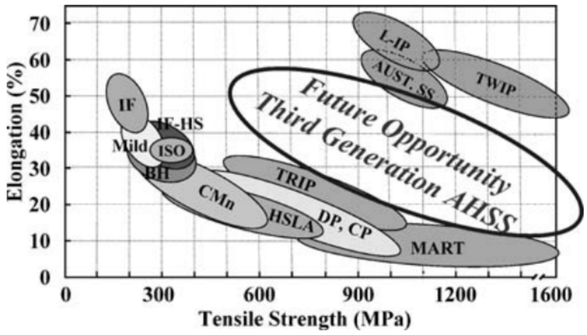

Figure 1.1: Strength and elongation data on conventional steel and different generations of advanced high strength steels (AHSS). [1]

Quenching and partitioning have been shown to provide a new class of AHSS. However, the use of this method has been far less documented for stainless steel. Martensitic stainless steel is often used for its desirable combination of strength and hardness and the inherent corrosion properties that stainless steel possesses. This is an improvement in mechanical properties in comparison with austenitic stainless steels which often lack strength and are not hardenable. However, these martensitic stainless steels often lack the desired ductility. This can potentially be solved by using the quenching and partitioning treatment on martensitic stainless steels to provide a better balance between the properties. The Q&P treated MSS could be an outcome to solve the increasing demand in fuel efficiency and safety standards for the automotive industry. Besides these two factors, the use of stainless steel can prolong the lifetime of cars, reducing the impact on the environment.

For conventional AHsS, the research in the validity of quenching and partitioning is mostly focused on the mechanical properties or microstructural development due to process parameter optimization. And for a good reason, the goal of this method is to achieve excellent strength and ductility. However, stainless steel is used in environments where conventional steels are not suited due to the corrosive environment. The microstructure will change due to the quenching and partitioning treatment, and microstructure optimization for mechanical properties has been the focus of recent research for MSS [4; 9; 10; 11]. The literature on what these changes in microstructure mean for the corrosion properties is lacking. While the focus of these developments is on the mechanical properties, the corrosion properties should not be negatively affected, as this will impact the possible uses of martensitic stainless steel in its industrial applications.

1.1 RESEARCH OBJECTIVE

This thesis is part of a research project named QPINOX, that aims to develop a new martensitic stainless steel suitable for lightweight automotive applications [12]. The new martensitic stainless steel has to achieve the second-generation AHSS properties in terms of strength and ductility, but also provide corrosion resistance, as discussed above. Corrosion properties of materials are the results of a number of factors, including the microstructure and composition of the material. The Q&P treatment will alter the microstructure of the material, and it is, therefore, important to evaluate the corrosion properties of these newly developed Q&P treated martensitic stainless steels. This thesis aims to experimentally determine the changes in corrosion properties caused due to the different Q&P parameters and different compositions of the materials used in the QPINOX project. The main research questions for this thesis are therefore as follows:

- How does novel quenched and partitioned martensitic stainless steel compare to commercial AISI 420 martensitic stainless steel in terms of corrosion performance?
- What is the influence of different phase fractions (primary martensite, fresh martensite and retained austenite) as a result of Q&P parameters on the corrosion properties of quenched and partitioned martensitic stainless steel? And what are the dominating microstructural features dominating these properties?
- How does manganese content influence the corrosion properties of quenched and partitioned martensitic stainless steel?

To answer these research questions, a combination of different experiments, both to research the microstructure and corrosion properties, will be used. Chapter 2 of this thesis will first give some theoretical background information on Q&P, and research from literature on corrosion properties of quenched and partitioned martensitic stainless steel. Because research on the corrosion properties of specifically Q&P treated MSS is limited, some important aspects of the microstructure and corrosion properties relation on Q&P treated AHSS, and quenched and tempered martensitic stainless steel will be discussed. These can potentially give an insight in to the dominating factors of Q&P treated MSS as well. The specific compositions of the alloys and the detailed Q&P parameters will be shown in Chapter 3. This chapter will also discuss the different experimental methods used to research the microstructure and corrosion properties. Chapter 4 will present the results obtained by these experimental methods, while Chapter 5 will form a discussion on these results and what they mean for the current state of Q&P treated MSS. To close out this thesis, Chapter 6 will present the conclusions and recommendations for future research in tothis topic.

2 THEORY AND BACKGROUND

In this chapter, a short overview of the quenching and partitioning treatment will be shown to familiarize the reader with the process and relevant parameters. After that, the current literature on corrosion properties of quenched and partitioned martensitic stainless steel and some literature on medium carbon steel, will be shortly discussed.

2.1 BASICS OF QUENCHING AND PARTITIONING

The quenching and partitioning process, as mentioned in the Introduction, is an integral part of this thesis. The thesis is focused on the microstructure and corrosion properties relation. The microstructure in question is acquired by the process of quenching and partitioning. The Q&P process was first described by Speer et al. [2; 8], and aims to reach a microstructure of martensite and retained austenite to provide a good combination of strength and ductility. The first step in the Q&P process is the full or partial austenitization of the sample, after which the sample is quenched to a temperature between the martensite start temperature (M_s) and the martensite finish temperature (M_f). The temperature chosen for the quench will determine the fraction of martensite formed after the primary quench and therefore also the fraction of austenite which is available to potentially stabilize. After the primary quench the sample is thermally treated to allow diffusion of the carbon out of the supersaturated martensite to austenite. This step is called the partitioning step. The carbon enrichment of austenite lowers the M_s temperature of the austenite, making it possible to be stable at room temperature. Finally, the material is quenched again. The carbon enriched austenite is now stable at room temperature (retained austenite) and, therefore, will not transform into martensite. The austenite that has not been enriched with carbon will transform into fresh martensite. The final microstructure will generally consist of primary martensite (formed at the first quench), retained austenite and sometimes fresh martensite. Figure 2.1 shows the schematic representation of a Q&P process.

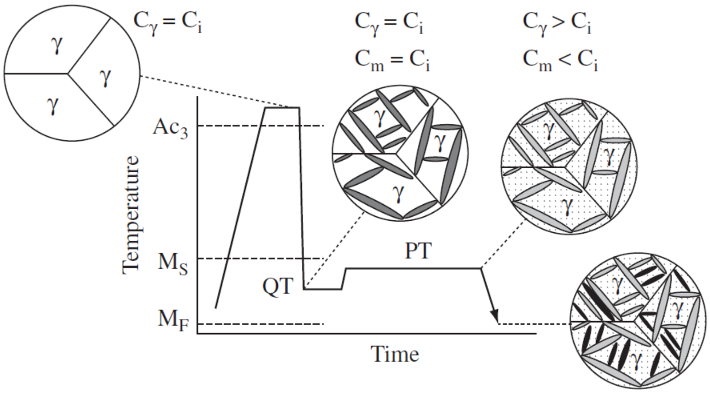

Figure 2.1: Representation of the Q&P process. QT and PT indicate the quenching temperature and partitioning temperature, respectively. C_γ, C_m and C_i indicate the carbon concentrations of austenite, martensite and the primary alloy, respectively.[2]

The parameters used in the Q&P process will partially determine the resulting microstructure. The quenching temperature, for example, will determine the fraction of primary martensite formed and, therefore, it will also determine how much austenite can be stabilized. Large amounts of primary martensite by quenching close to the M_f temperature will mean that there is a lot of supersaturated martensite with high amounts of carbon available for partitioning. However, this also means there is a low fraction of austenite which can be stabilized, resulting in low values of retained austenite. On the other hand, quenching close to the M_s temperature will yield a low fraction of primary martensite. This can cause a situation where not enough carbon is available to stabilize the remaining austenite [7]. Both situations would lead to a microstructure dominated by primary or fresh martensite, and not enough desired retained austenite. This determination of quench temperature (but also of partitioning temperature and time) will therefore be important for the final microstructure. For this thesis, the values of these parameters have already been determined in earlier research [4]. A careful selection of parameters has been chosen to yield four different samples with different phase fractions. These will be further discussed in Chapter 3.

The thermodynamics of the partitioning step is important for the theoretical understanding of the process. By understanding the theory behind the process, the process parameters can be chosen to get the desired microstructure. Parameters like quenching temperature, partitioning temperature and time all influence the microstructure, as discussed before. Speer et al. [2; 8] proposed a model of carbon partitioning and called it constrained para-equilibrium (CPE). This was later revised by Hillert and Årgen to constrained carbon equilibrium (CCE) [13; 14]. A constrained equilibrium means that the temperature is not high enough to cause diffusion of the iron atoms or substitutional atoms (at least not in a reasonable time scale). The diffusion of interstitial atoms, however, requires much less energy, and they are therefore still mobile at these temperatures [15]. This gives rise to two constraints in the CCE model. Firstly, carbide formation is completely suppressed and the martensite/austenite interface is immobile. This implicates that there will be no other reactions competing for carbon. The formation of carbides or bainite, for example, would indicate the consumption of carbon atoms. These would then not be available for the enrichment of the austenite. This constraint also restates what is mentioned before, namely that there will be no movement of iron atoms or substitutional atoms, fixing the martensite/austenite interface. Second, the diffusion of carbon is complete once the chemical potential of carbon in both austenite and martensite are equal. The difference in the chemical potential of atoms in different phases is a driving force for diffusion. So the model describes the end of the partitioning step at the moment that the chemical potential of carbon is equal in martensite and austenite. Figure 2.2 shows a Gibbs free energy curve of two phases (ferrite and austenite) in a Fe-C system. Two compositions are indicated in which the chemical potential of carbon is equal, and therefore the end of the partitioning is reached.

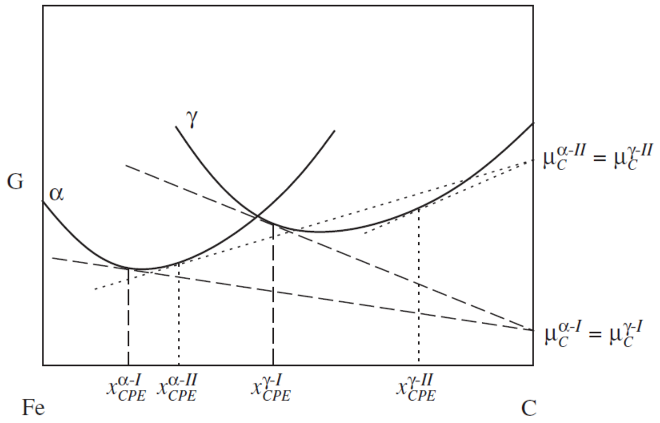

Figure 2.2: Gibbs free energy curve with the chemical potential of carbon represented in two phases (in this case ferrite and austenite) with tangent lines. Two possible compositions are shown at the end of the partitioning steps, since the chemical potentials of carbon are equal. [2]

The Q&P treatment has been shown to yield good results for the development of new AHSS. There are several commercial Q&P steels already available with good strength and ductility, and improvement of Q&P steels is constantly developing [16]. However, the constraints of the CCE model are not always fulfilled. From Figure 2.2 it can be seen that in this situation, the chemical potential of the iron atoms is not equal (the tangent lines for both phases can be extended to the left vertical axis to represent the chemical potential of iron). This implies that there is a driving force for the martensite/austenite interface to move until it reaches full equilibrium. Besides the motion of the martensite/austenite interface, there is also a risk of carbide formation at longer partitioning times. This, in turn, reduces the amount of retained austenite that is present in the final microstructure [17].

2.1.1 Quenching and Tempering vs. Quenching and Partitioning

At first sight, Q&P might seem to be very similar to quenching and tempering (Q&T), but there are crucial differences between the two processes. Since Q&T will often be used in this thesis to form some hypotheses, a very short description will show the differences between Q&P and Q&T. In the Q&T process, quenching is always done to room temperature to form a martensitic structure with very low fractions of austenite. This is essentially different from Q&P, where quenching is done to an intermediate temperature between M_s and M_f to provide a specific fraction of austenite that later will be stabilized. After quenching to room temperature, tempering is used to regain ductility in the material. The remaining austenite in the Q&T steel is expected to eventually decompose in ferrite and carbides during the tempering step. The carbide formation in tempered steels will start fairly early on in the tempering step in the form of transition carbides but will eventually grow in cementite like carbides [15]. For stainless steel, the new carbides that are formed are often reported to be Fe_2C, $M_{23}C_6$ or M_7C_3, where M can stand either for Fe atoms or Cr atoms [18; 19; 20]. So clearly, in Q&T the occurrence of carbon competing processes is expected to happen, especially carbide formation is common. Also, no austenite is expected to be present in the final microstructure. The only phases left are tempered martensite, ferrite and carbides. In quenching and partitioning, the carbon from the supersaturated martensite is expected to only be used to stabilize austenite, so no decomposition of austenite into other phases, or carbide formation will happen. The final microstructure will be expected to only consist of primary (tempered) martensite, retained austenite and fresh martensite.

2.1.2 Addition of Manganese in Q&P steels

Manganese is often used in steels to promote austenitic microstructures. This element causes the phases transformation of austenite to ferrite to happen at much lower temperatures. Manganese lowers the free energy of austenite when compared to ferrite, stabilizing the phase [15]. In previous research by Benne de Bakker[4], it was already shown that manganese in quenched and partitioned martensitic stainless steel greatly increases the fraction of retained austenite. While manganese is beneficial for stabilizing austenite, it can be detrimental for corrosion properties in the form of manganese-sulfide (MnS) inclusions or other manganese rich inclusions. Stainless steel, in general, is very resistant to overall corrosion but suffers from localized attacks like pitting corrosion. The presence of secondary phase particles or carbides can lead to chromium depleted zones in the steel matrix, causing preferable pitting initiation sites [21; 22]. This addition of manganese, therefore, becomes an important factor in corrosion properties of Q&P treated MSS and is one of the major research questions in this thesis.

2.2 THE INFLUENCE OF QUENCHING AND PARTITIONING ON CORROSION PROPERTIES

Microstructural features like phase fractions, carbides, grain size and composition of the material dictate the corrosion resistance of a material. Quenching and partitioning is a treatment that changes the microstructure significantly. While this treatment is mostly focused on optimizing the mechanical properties, the change in microstructure will inevitably cause changes in the corrosion properties of the material. It is therefore important to research the effect of thermal treatments like quenching and partitioning on the corrosion resistance of steel. However, the literature on the corrosion properties of quenched and partitioned martensitic stainless steel is very limited at the time of writing. The only literature available which considers specifically the impact of Q&P on the corrosion properties of MSS is research by Lu et al.[3], Dieck et al.[23] and research on cavitation corrosion/erosion of Zhou et al. [24]. However, because cavitation is a phenomenon more based on mechanical properties (and the focus of the corrosion in this report is of an electrochemical kind), it is considered out of the scope of this work. Both Lu et al.[3] and Dieck et al.[23] compare quenched and partitioned martensitic stainless steel with quenched and tempered martensitic stainless steel. Mainly the research by Lu et al.[3] will be used to give an overview of the current literature.

Lu et al.[3] investigated the corrosion properties of martensitic stainless steel (30Cr13) with composition 0.28C, 0.60Mn, 0.35Si, 13.0Cr and balance Fe, all in wt%. Samples of this steel were first austenitized at 1130°C for 30 minutes and then quenched into a salt bath of 220°C for 5 minutes. Samples were then partitioned at different partitioning temperatures ranging from 300 to 500°C for 30 minutes and finished by an oil quench. The quenched and tempered samples were also austenitized at 1130°C for 30 minutes, and then quenched to room temperature. After the quench, the samples were tempered at temperatures ranging from 300 to 500°C. The full microstructural development during the Q&P treatment can be found in [3].

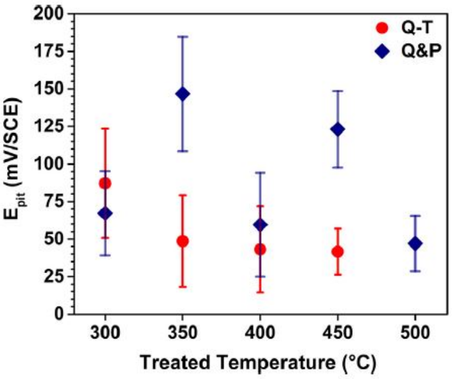

Figure 2.3: Pitting or breakdown potential (E_{pit}) for Q&T and Q&P treated samples, based on the potentiodynamic polarization curves (30Cr13). [3]

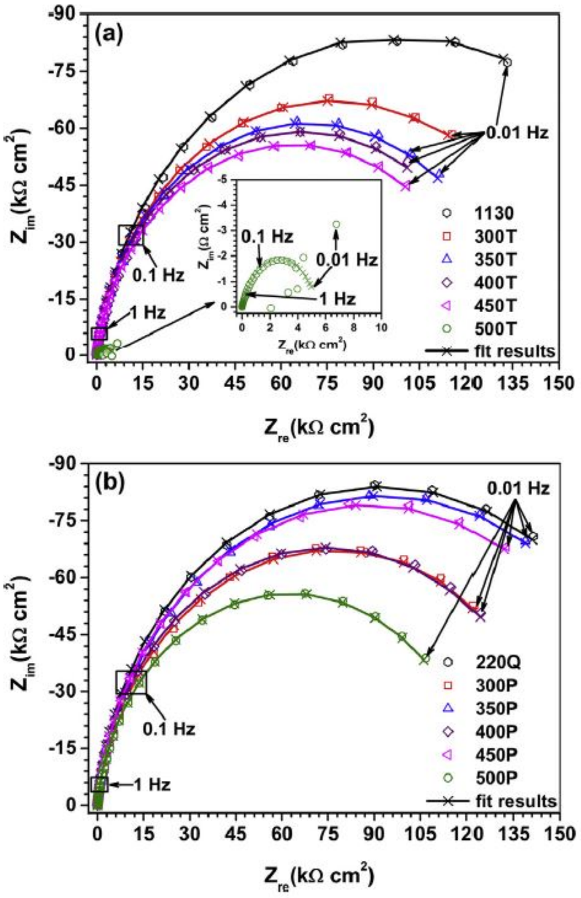

Figure 2.4: Nyquist plot for (a) Q&T samples and (b) Q&P samples in 3.5 wt% NaCl aqueous solution at room temperature (30Cr13). [3]

In this research, the authors show that the Q&P treated samples show a comparable, or even increased corrosion performance when compared to Q&T treated samples. Especially the pitting potential (E_{pit}) is increased for the 350P and 450P samples as shown in Figure 2.3. The 350P and 450P samples have a retained austenite fraction of 10.41 ± 1.49 vol% and 8.62 ± 0.39 vol%, respectively. However, the interesting observation is that the 400P sample with the highest retained austenite fraction (13.06 ± 0.39 vol%) does not outperform its tempered counterpart. This indicates that the fraction retained austenite does play a role in the superior corrosion performance of Q&P treated steel, but is not the only factor.

The EIS results show a similar trend when compared to the pitting potentials. The full fitting parameters can again be found in [3]. Notable in these nyquist plots, however, is the fact that the quenched samples show the best passive film properties by having the largest arc radii. The reason for this is most probably due to the fact that these samples will contain less, or no carbides in their microstructure. Carbides can form cathodic areas and impact passive film properties. In Q&T samples, the carbides formed can even be in the form of $M_{23}C_6$ or M_7C_3 and greatly decrease corrosion properties [19; 25]. This is caused by areas of chromium depletion due to chromium consumption of these carbides. The presence of carbides is therefore important for corrosion properties and one of the arguments by Lu et al.[3] for the improved corrosion properties of Q&P samples.

Dieck et al.[23] came to the same conclusion, their partitioned samples also showed improved corrosion resistance when compared to tempered samples. However, they also showed the importance of austenitization temperature in quenching and partitioning. In their samples, chromium-rich carbides were still present. They theorized that these carbides were still present from before the Q&P treatment, lowering the corrosion performance. Lu et al.[26] showed that the austenitization performance is important to be able to dissolve all carbides, and confirms that the austenitization temperature of Dieck et al.[23] could have impacted their research into the corrosion properties.

Overall, the research in quenched and partitioned martensitic stainless steel show that the corrosion performance is at the very least comparable, and in most cases even superior to quenched and tempered martensitic stainless steel. Most of this is attributed to the absence of chromium-rich carbides. Research in the corrosion performance of conventional Q&P steel has also shown some trends that can be useful for the research in martensitic stainless steel. Mehner et al.[27] showed in their research in to corrosion of Q&P treated medium carbon steel that once again the Q&P treated samples outperformed Q&T samples. However, this was only true in neutral conditions (0.1 M NaCl). In acidic solution (0.25 M H_2SO_4) the opposite was true, Q&T showed improved corrosion resistance compared to Q&P. The improved corrosion performance of Q&P samples in neutral conditions in this research is, aside from the carbide argument, attributed to the formation of galvanic cells. The authors argue that the different phases can form micro-galvanic cells, but for the Q&T samples the cathodic area is much larger than for the Q&P sample, increasing corrosion rate. The switch in corrosion rate between Q&P and Q&T is not well explained, but the possible formation of micro-galvanic cells could be a factor in martensitic stainless steel as well. Lastly, Yang et al.[28] also considered corrosion performance of Q&P treated medium carbon steel. They once again found superior corrosion properties in Q&P steel compared to Q&T steel. They attributed the superior corrosion performance to the difference in residual stresses. Normally martensitic structures have high residual stresses, Yang et al.[28] argue that the large fractions of retained austenite can accommodate the shape change of the martensitic transformation and lower the residual stresses in martensite. Lower residual stresses lead to lower free energy and indirectly to better corrosion properties. The shape and fraction of retained austenite could therefore also be important for corrosion properties of quenched and partitioned martensitic stainless steel.

3 MATERIALS AND METHODS

This chapter will discuss the materials and the experimental methods used in the current thesis. First of all, the different alloys of martensitic stainless steel are discussed. Then for the Q&P treated materials, the quenching and partitioning treatment will be shown with the exact parameters used, and resulting phase fractions will be discussed. After the materials, the various experimental methods that were used in this research will be discussed.

3.1 MATERIALS: MARTENSITIC STAINLESS STEEL ALLOYS

For this research, three different alloys of martensitic stainless steel were used. First of all, as a baseline material to compare corrosion performance of the new Q&P treated alloy, commercial AISI 420 martensitic stainless steel was chosen. The composition can be found in Table 3.1. The as-received state of this steel is annealed. The Q&P treated martensitic stainless steel used in this research has two different compositions. One alloy has low manganese content (samples QP1 and QP2), the second has a high manganese content (samples QP3 Mn and QP4 Mn). Both compositions can also be found in Table 3.1.

Alloy	C	Si	Cr	Mn	Fe
AISI 420	0.4	0.35	14	0.7	bal.
Low Mn QP (QP1 and QP2)	0.2	0.35	12.5	0.7	bal.
High Mn QP (QP3 Mn and QP4 Mn)	0.2	0.35	12.5	3	bal.

Table 3.1: Chemical composition of the three studied alloys. All elements are in wt%.

While there are significant differences between the AISI 420 steel and the QP steels in terms of carbon and chromium, it is still valuable to compare the corrosion properties of both. One of the research questions is how quenched and partitioned martensitic stainless steel compares to commercial martensitic stainless steel in terms of corrosion performance. For this reason the AISI 420 was chosen as it is commercially widely available.

3.2 THE QUENCHING AND PARTITIONING PARAMETERS

The Q&P treated samples used in this study were received in a quenched and partitioned state. However, to ensure the results can potentially be reproduced in the future, and to support the resulting phase fractions, a short description of the heat treatment is given.

The as-received material (hot rolled, and annealed for 24 hours at 600°C) was first heated at 10 °C/s to an austenitization temperature of 1100°C, and held at this temperature for 15 minutes, after which the material was cooled to room temperature with a cooling rate of 5°C/s. After the austenitization the material was subjected to the quenching and partitioning heat treatment. All samples were first heated at 10°C/s to the austenitization temperature, and then quenched to different quenching temperatures with a cooling rate of 5°C/s after which they were held at this temperature for 20 seconds. The different quenching temperatures for each sample can be found in Table 3.2. The samples were then reheated to a partitioning temperature of 450°C at a heating rate of 10°C/s and held at this temperature for 5 minutes. After the partitioning step was completed, the samples were quenched to room temperature at a cooling rate of 5°C/s. The partitioning conditions were based on previous research on martensitic stainless steel, and aimed to avoid the formation of stable $C_{23}C_6$ carbides [4].

Sample	Quenching Temperature [°C]
QP1	135
QP2	170
QP3 Mn	133
QP 4 Mn	168

Table 3.2: Quenching temperatures and phase fractions of the different samples. Phase fractions are shown in percentage.

3.3 EXPERIMENTAL METHODS

In this section, all experimental methods will be discussed. First the sample preparation will be discussed that is required for most experiments. After this, several microstructural and electrochemical experiments will be discussed. The SKPFM technique will be shown in slightly more detail, as this technique is not as widely used as the other methods in this section.

3.3.1 Sample preparation

All of the experimental methods discussed in this section require a certain basic sample preparation procedure. The samples were received in their quenched and partitioned state, in a cylindrical shape with varying lengths and a diameter of 4mm. This shape is chosen due to the use of dilatometry to achieve the desired heat treatment. The AISI 420 samples were received as square-shaped samples measuring 10x10 mm and 3mm in thickness. All samples were mounted in non-conductive resin to allow easier handling and use in experiments. Important to consider is that the resin has to be non-conductive for the electrochemical experiments. This is not ideal for EDS and EPMA analysis, but since there was a work-around to still make the samples conductive for this technique, the choice was made to mount all sample in non-conductive resin. After mounting, all samples were sanded with SiC sanding paper in progressively finer grit sizes down to grit 2000. After sanding, the samples were cleaned in isopropanol using an ultrasonic cleaner for 5-10 min. To acquire a defect-free, mirror finish, the samples were then polished using 3 and 1 µm polishing liquid and cloths. After polishing, the samples were rinsed with isopropanol, and cleaned in isopropanol using ultrasonic cleaning for

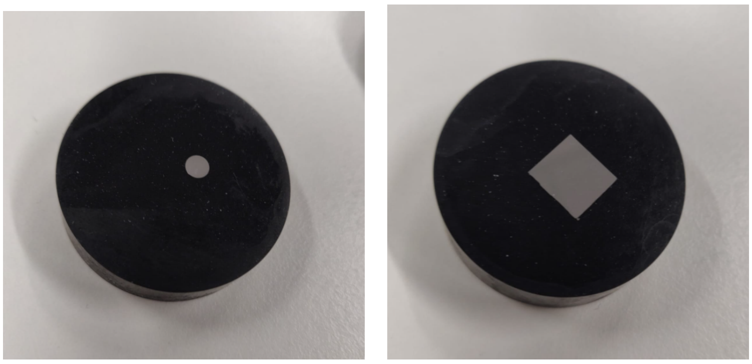

(a) (b)

Figure 3.1: Mounted Q&P (a) and AISI 420 (b) sample.

at least 10 min. This sample preparation was done before all experiments. Figure 3.1 shows a Q&P sample, and an AISI 420 sample which have been mounted in resin, and polished down to 1 for a mirror-like finish. Potential additional sample preparation for specific experiments is explained at the start of each subsection describing the experiment.

3.3.2 Optical Microscopy and Etching

Optical microscopy was used in this project to characterize the microstructure of different samples. The main microscope used was the digital Keyence VHX-5000, some additional images were made using a LEICA DMLM optical microscope. The software of the Keyence microscope was also used to measure the areas of samples before conducting the electrochemical experiments. Application of lacquer (described in the electrochemical experiments section) caused the area of each sample to be different. The Keyence software can easily measure this area as shown in Figure 3.2.

Etching of the samples was done using Vilella's reagent. The etchant is given in ASTM standard E 407 [29]. All samples were etched by swabbing etchant onto the sample surface for 20-50 seconds. The etch time depends on the type of sample, each sample was first etched for 15 seconds and then visually inspected under optical microscope. If more etching was necessary, steps of 5 seconds swapping was done until the desired microstructure became clearly visible. After each etching step the sample was thoroughly rinsed with isopropanol.

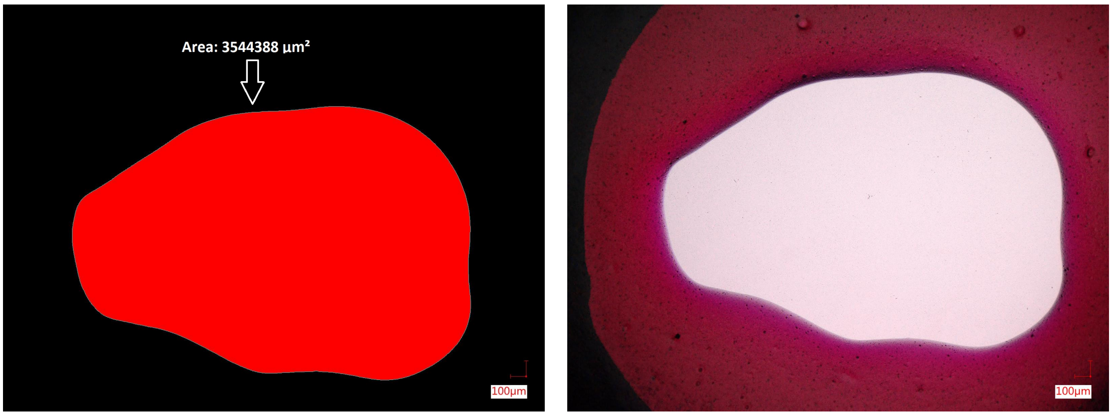

(a) (b)

Figure 3.2: Area calculated by Keyence software (a), and micrograph of sample with laqcuer (b).

3.3.3 Electron Probe Micro-Analysis (EPMA) and Energy Dispersive X-ray Spectroscopy (EDS)

To show the elemental banding and distribution of the samples, EPMA was used. Qualitative maps of the element distribution were measured using a JEOL JXA 8900R electron probe microanalyzer. The electron beam had an energy of 10kV and a beam current of 500 nA using wavelength dispersive spectrometry (WDS). Each element can then be determined by using its X-ray intensity compared to the X-ray intensity of reference materials. The detection limit and counting error of each measured element can be found in Table 3.3.

Quantative linescans on the samples using Energy Dispersive Spectroscopy (EDS) was done to show the precise wt% of each element in the sample. The linescans were made using a SEM JEOL JSM-6500F with a beam energy of 15kV and current of 0.6 nA. Data acquisition for Energy Dispersive Spectroscopy (EDS) was performed with a ThermoFisher NSS system using a UltraDry detector with 30 mm^2 detector surface.

Element, X-ray line	Energy [kV]	Detection Limit [ppm]	Counting error [wt%]
Carbon, C Kα	0.282	50	0.15
Silicon, Si Kα	1.740	15	0.03
Chromium, Cr Kα	5.474	50	0.20
Manganese, Mn Kα	5.898	50	0.20

Table 3.3: Energy and detection limit for each element analyzed.[4]

3.3.4 Electrochemical Experiments

To show the overall corrosion performance, several electrochemical experiments were performed. Before conducting the electrochemical experiments, part of the sample surface was masked off by applying lacquer to prevent possible crevice corrosion from happening at the material/resin interface. An example of a masked sample can be seen in Figure 3.2b. The electrochemical experiments were all performed using a Biologic VSP-300 potentiostat, supported by EC-Lab V11.36 software. The experimental setup was a three-electrode cell, using a Ag/AgCl (saturated KCl) electrode as a reference electrode, a platinum mesh as a counter electrode and the sample surface as the working electrode. A 3.5wt% NaCl aqueous solution was used as the electrolyte. The reference electrode and counter electrode were carefully placed so they were not touching each other, which could otherwise lead to faulty data. Both the three-electrode setup, and the orientation of counter and reference electrode can be seen in Figure 3.3. The working electrode, or sample, is clamped under the red part of the cell. With the use of an o-ring, a seal is made so the electrolyte can be poured into the cell and only part of the whole sample is exposed.

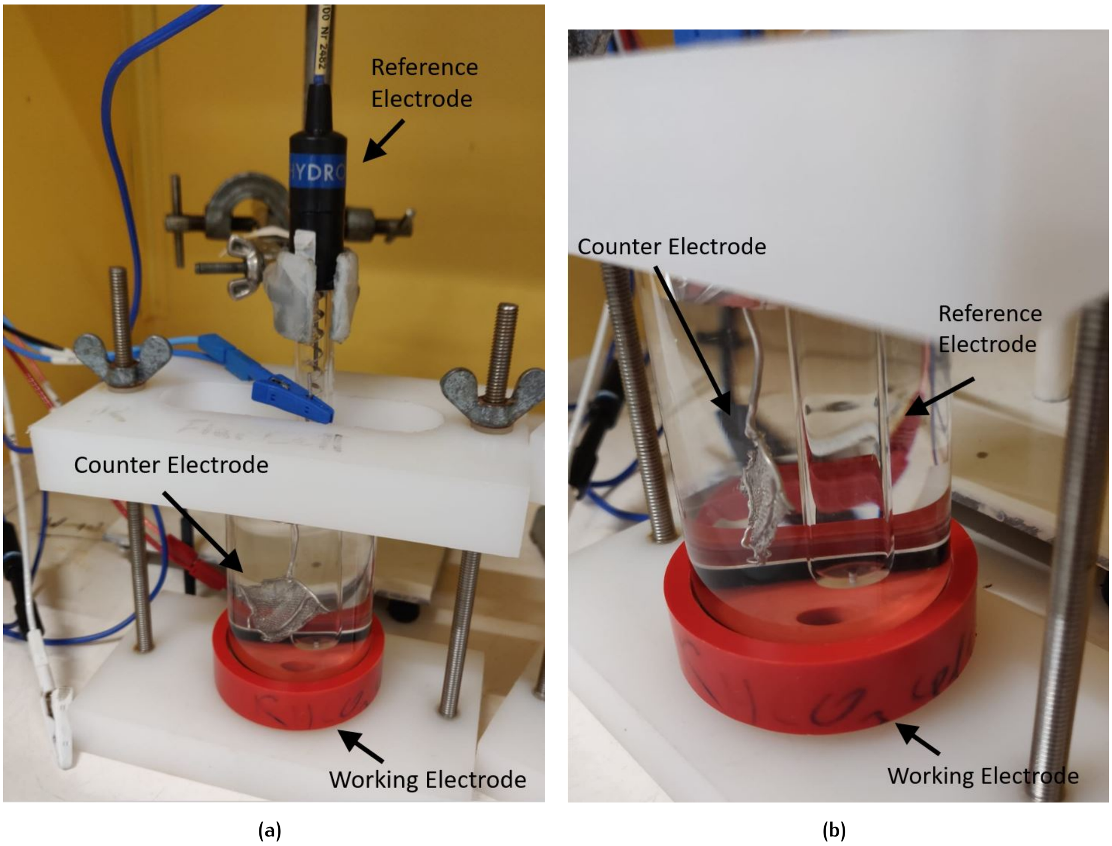

(a) (b)

Figure 3.3: Three-electrode setup (a). Positioning of counter and reference electrode (b).

First, cathodic polarization was used to remove the passive film of each sample at -300mV vs OCP for 30 minutes. Cathodic polarization is used to strip the material of its passive film, to allow reformation of this passive film during the OCP measurement. While there are not many conclusions that can be drawn from this data, it can show if there are any errors in the experimental setup. The figure shown in Figure 3.4 is a cathodic polarization plot that shows typical behaviour during this step. The current will initially drop, and then over time rise, to an almost constant value. If the plot shows large fluctuations in current, or other unexpected behaviour, this can be an indication that there is an error in the experimental setup. There could, for example, be penetration in the lacquer that is covering part of the sample, or the presence of an air bubble on the sample surface. Especially air bubbles on the surface resulted in heavily distorted cathodic polarization plots, which then indicates that the data of the experiment will not be reliable. For all datasets that were eventually used to describe the behaviour of the material, a check has been done on the cathodic polarization as well. If the cathodic polarization was distorted in any way, the data was deemed to be unusable.

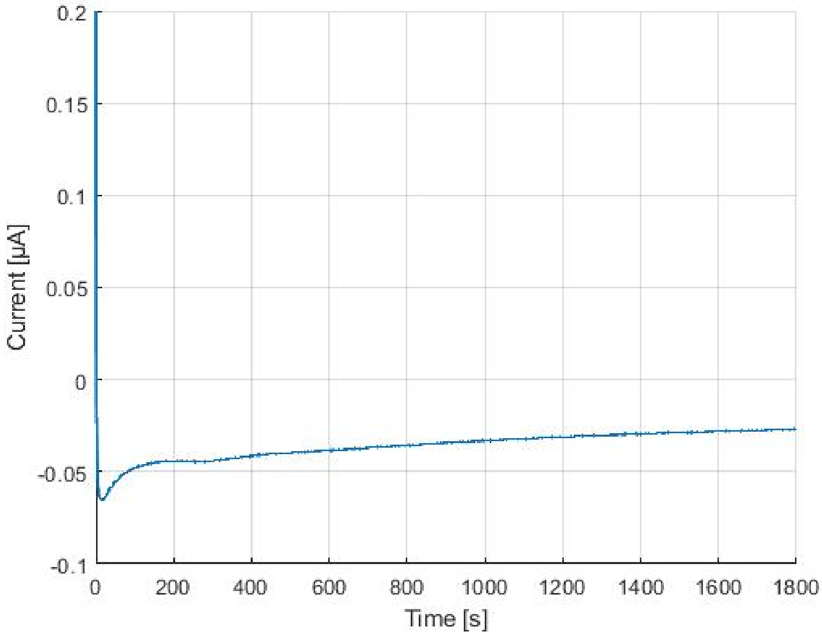

Figure 3.4: A typical cathodic polarization curve for all MSS samples. This curve belongs to one of the QP3Mn samples.

After cathodic polarization, the Open-Circuit Potential was measured. The OCP was measured for 1.5 hours to ensure the potential stabilizes to a constant value. The OCP is mainly used as a basic potential for the Potentiodynamic Polarization and Electrochemical Impedance Spectroscopy (EIS), but there will also be some observations that can be made from the development of the OCP. EIS measurements were done using an amplitude of 10mV and a frequency range of 30 kHz to 0.01 Hz. The data of this measurement will be presented as both Nyquist and Bode plots, including fitting with an equivalent circuit. Lastly, potentiodynamic polarization was done to show the behaviour of the material, until pitting occurred. The scan was made from -100mV vs. OCP to 500mV vs. OCP with a scanrate of 0.166 mV/s. All potentiodynamic polarization plots will be presented in terms of current density. In other words, the current will be normalized to surface area. Since each sample is painted with lacquer, the areas can differ greatly. To make sure the potentiodynamic polarization plots are comparable, normalizing to surface area of the sample is important..

3.3.5 Scanning Kelvin Probe Force Microscopy (SKPFM)

The above mentioned electrochemical experiments give a general overview of the corrosion properties of the material. By changing for example phase fractions or the manganese content, the influence of these changes can be seen in the electrochemical experiments. However, to gain more information about the microstructural features and their overall nobility in the material, SKPFM can be used.

SKPFM is, in essence, a combination of the atomic force microscope (AFM) and the scanning Kelvin probe (SKP). During SKPFM (lift mode), the tapping mode of AFM is used to create a topography map during the forward scan. In AFM tapping mode, a cantilever with nanometer-scale tip is oscillates at a constant frequency. When this tip is brought near the sample surface, interactive forces between the sample and the tip cause this oscillation frequency to change. This change in oscillation frequency is what produces a topography map of the surface. In the backwards scan, the tip is lifted (hence the name, lift mode) to around 100 nm off the surface. This distance can be changed and is a parameter of the SKPFM scan. The tip then measures the Volta-potential between the tip and the surface. With this method, the topography of the surface, together with the nobility of certain microstructural features can be mapped in one technique. This is an advancement on the more classic scanning Kelvin probe (SKP) because the addition of a layer of electrolyte is no longer needed. SKPFM can be done in ambient air conditions.[30]

The Volta-potential gives information about the nobility of the sample surface. When two dissimilar metals (one will be the Kelvin probe, the other the sample or metal surface) with different Fermi levels (E_f) are brought in contact, their Fermi levels will equalize (Figure 3.5 (a) & (b)). This causes a flow of electrons from the metal with low Work function to the metal with high Work function. This equalizing of the Fermi levels of the two metals causes a difference in potential between the vacuum levels. This difference in potential is the Volta potential. And external bias is then applied between the probe and the metal to equalize these vacuum levels to their original positions. Therefore shifting the

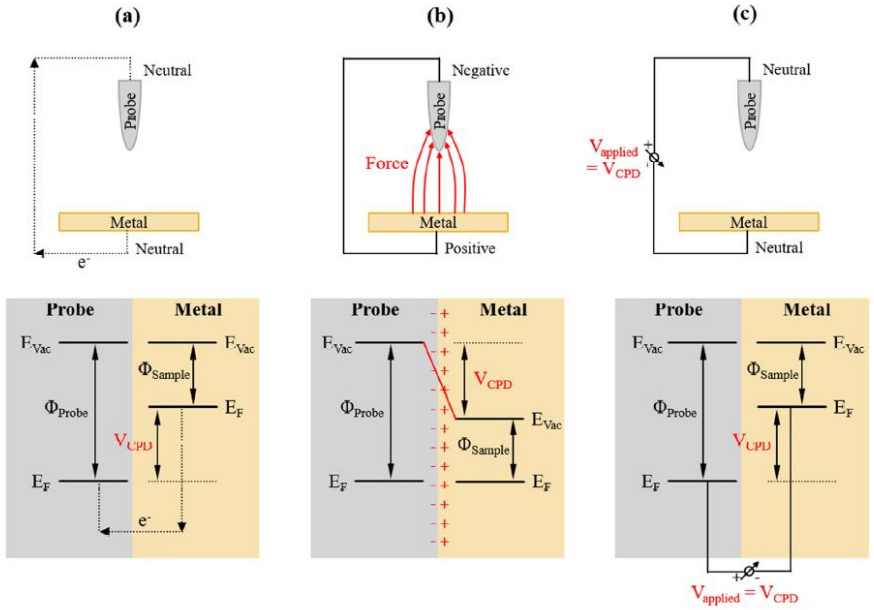

Figure 3.5: Working principle of the SKPFM Volta-potential measurement. (a) Two dissimilar metals (Probe and sample) are brought in contact, (b) the Fermi levels (E_F) equalize causing an electron flow and difference in vacuum levels (E_{vac}) which is equal to the Volta potential, (c) The applied bias equalizes the vacuum levels again.

Fermi levels again, and causing the materials to be uncharged.[30; 31]

The Work function describes how much energy is needed to remove an electron from the Fermi level, and move it to the vacuum level. In other words, it gives an indication of the tendency for electron transfer at the surface. Since electron transfer is a crucial aspect of corrosion, the Work function can therefore describe the nobility of materials. The Volta potential is described in the review by Örnek et al. [30] to be linearly proportional to the Volta potential. However, to relate the Volta potential to the nobility of the phases that are measured, it is important to check in what way the bias is applied. The difference between tip and sample bias can be shown with two equations [30]:

$$\psi_{Me} = \psi_{Pt} - V_{CPD} \tag{3.1}$$

$$\psi_{Me} = \psi_{Pt} + V_{CPD} \tag{3.2}$$

Where ψ_{Me} is the Volta potential of the metal sample, ψ_{Pt} is the Volta potential of platinum (in this case the tip material is platinum, which is a frequently used tip material) and V_{CPD} which is the measured Volta potential difference. Now let's say that the measured area is a more cathodic area with a high Work function and thus high Volta potential difference (V_{CPD}). This then means that the overall Volta potential of the metal (ψ_{Me}), in the case of tip bias, becomes low, according to Equation 3.1. However, if the sample is biased (Equation 3.2), the Volta potential of the metal (ψ_{Me}) will be high for a cathodic area. This shows that the applied bias is very important for the interpretation of the data. The interpretation for high potentials in corrosion research normally indicates cathodic areas, but for SKPFM, care should be taken since the tip/sample bias can flip the interpretation of this potential.

In this thesis, SKPFM measurements were performed on a Bruker Dimension Edge AFM using an SCM-PIT-V2 tip (platinum-irridium coated tip). Samples were, aside from polishing to 1 µm as described earlier, polished with Struers OP-S (0.25 µm polishing liquid. The tip lift height was kept at 100 nm and a bias potential of 6V was applied, copper tape was applied to establish electrical contact with the sample. In these measurements, a tip-bias was applied. So high Volta-potential in the SKPFM results will result in more anodic features, and low Volta-potentials result in more cathodic features.The measurements were taken at ambient air temperatures of 22°C. The data was processed using Gwyddion software (version 2.59).

4 RESULTS

This chapter will discuss the results that were acquired during the experimental work of this research. The chapter will mainly be divided into two parts. The first part will discuss the results of the microstructural characterisation that were listed in Chapter 3, and the second part will discuss the electrochemical characterisation.

4.1 MICROSTRUCTURE CHARACTERIZATION

To gain more insight into the relation of microstructure and corrosion performance of Q&P treated MSS, experiments to reveal the relevant microstructural features are important. First of all the optical microscopy (OM) results will be shown. This will be followed by quantitative linescans performed by EDS and qualitative maps performed by EPMA, to show elemental distribution. Lastly, the samples were analyzed using Scanning Kelvin Probe Force Microscopy (SKPFM).

4.1.1 Microstructure analysis

Micrographs of the resulting microstructures after etching are shown in Figure 4.1. For all samples, the microstructure clearly is dominated by martensite laths, as expected. Retained austenite is, however, not easily distinguished in optical microscopy. The blocks of retained austenite are very small and are only exposed when using techniques like EBSD. Earlier research [4] has shown that the retained austenite is (as expected) mainly located at the primary martensite, as seen in Figure 4.2. This figure also shows how small the retained austenite blocks are, once again showing that they can not be seen in the optical micrographs of Figure 4.1. It is also hard to distinguish the two different kinds of martensite in samples QP1, QP2 and QP3 Mn. For these samples the fractions fresh martensite are fairly low, making it almost impossible to distinguish the different martensite phases in the micrographs. The phase fraction resulting from the quenching and partitioning treatment as described in section 3.2 are given in Table 4.1. The phase fractions are based on the dilatometry data of [4].

Sample	Primary Martensite	Retained Austenite	Fresh Martensite
QP1	84.7	11.1	4.2
QP2	73.6	20.8	5.6
QP3 Mn	68.1	25	6.9
QP 4 Mn	43.1	8.3	48.6

Table 4.1: Phase fractions of the different samples. Phase fractions are shown in percentage.

Sample QP4 Mn, however, has a fraction of 48.6% fresh martensite. Due to this high fraction, a distinction can be made from the micrograph in Figure 4.1d. This micrograph shows a distinct difference between a darker martensite phase, and a light martensite phase. Since etching is a form of selective dissolution, different phases will be etched at different rates. Since the fresh martensite has a higher concentration of carbon compared to the initial martensite, this phase will etch to a lesser extend. This causes the difference in color in the micrographs. The initial or tempered martensite (M1) has a darker color, having contained less carbon it has been etched more. The fresh martensite (M2), containing more carbon and thus acting more cathodic, will etch to a lesser extend, having a lighter

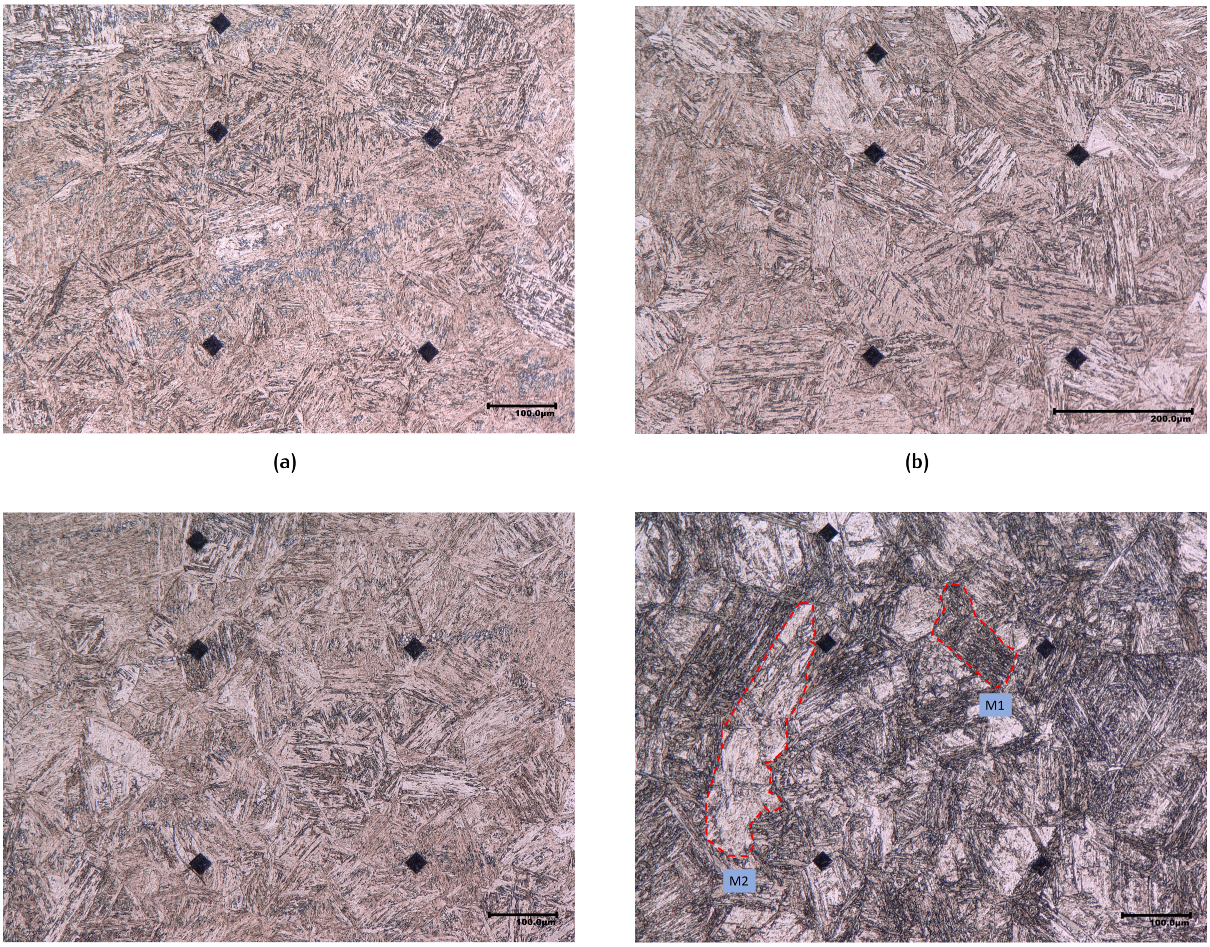

(a) (b)

(c) (d)

Figure 4.1: Optical micrographs of etched samples, all etched with Vilella's reagent. (a) QP1 (b) QP2, (c) QP3 Mn (d) QP4 Mn with indications of primary (M1) and fresh (M2) martensite.

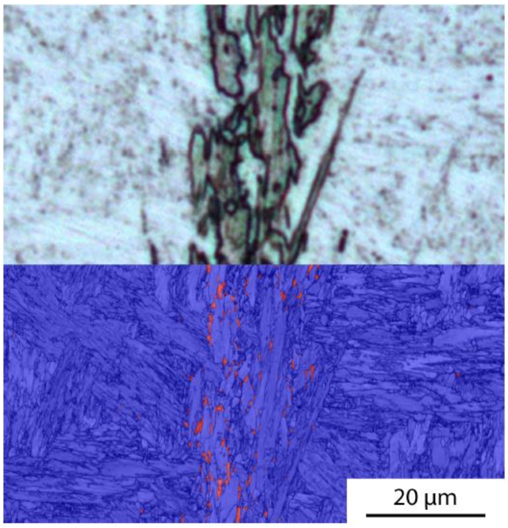

Figure 4.2: Optical micrograph (top) and EBSD phase map (bottom) of Q&P sample with high Mn quenched to 156°C. Red shows retained austenite and blue shows martensite. Adapted from [4].

color. Sample QP4 Mn also showed a significant banding structure of phases. This has already been shown to be a result of the rolling direction of the prepared samples [4].

4.1.2 Elemental Distribution

Energy Dispersive X-ray Spectroscopy (EDS) and Electron Probe Microanalysis (EPMA) can give important information about the elemental distribution of the material. This elemental distribution could influence the corrosion properties, and is therefore an important part of the microstructural research. As already mentioned in the previous subsection and in previous research [4], there is a banding structure present in the samples. This is most likely caused due to banding in the elemental composition, EDS/EPMA can show this potential banding or the presence of seconday phase particles.

Energy Dispersive X-ray Spectroscopy was used to make linescans on the sample surfaces to quantitatively determine the elemental distribution in the samples. This technique gives an accurate view of the amount of certain elements in wt%, with micrometer precision. Figure 4.3 shows the quantitative elemental distribution of chromium, manganese and silicon for all four samples. While the average chromium content of the alloy is 12.5 wt% chromium, Figure 4.3 shows that there are fluctuations as high as ±1.5 wt%. Depending on the sample, there are measurements as low as 11.4 wt% (QP3 Mn, Figure 4.3c) and as high as 13.9 wt% (QP2, Figure 4.3b).

The EDS measurements for the high manganese samples (QP3 Mn and QP4 Mn) also show the precipitation of particles that are rich in both manganese and silicon. In both Figure 4.3c and Figure 4.3d spikes in manganese and silicon content are visible. Manganese content is locally increased up to 9.5 wt%, and silicon up to 3.4 wt% for sample QP3 Mn. For sample QP4 Mn, manganese is increased locally to 6.8 wt% and silicon to 0.98 wt%. This indicates that some form of manganese silicide precipitates during the Q&P treatment in the high manganese samples. The EDS measurements can not directly determine the size of these particles with high precision. The measurements were done with a step size of 6 µm, and the particles in QP3 Mn and QP4 Mn are visible within two steps of the measurement. This indicates that the particle size will be smaller than at most 12 µm. Besides the presence of manganese silicide, these spikes in manganese can also be an indication of manganese sulfide (MnS) inclusions.

Electron Probe Microsanalysis (EPMA) was used to show qualitative elemental distribution maps of the samples. Figure 4.4, Figure 4.5, Figure 4.6 and Figure 4.6 show the qualitative elemental distribution maps of samples QP1, QP2, QP3 Mn and QP4 Mn, respectively. The maps show the elemental concentration in certain colours, running from blue to green to red/pink, with blue representing low concentration and red/pink high concentration. For the chromium maps, all samples except QP3 Mn show the average concentration of 12.5wt% as green. For sample QP3 Mn, this is represented as yellow/orange. Each colour in the maps is attributed a value in the EPMA analysis, considering these values a deviation of 12% from the average can be determined. Taking in to consideration that 12.5 wt% is the average composition of chromium, there are fluctuations of 1.5 wt% in the chromium concentration. This is well in line with the linescans acquired by EDS. As expected, all samples show a clear banding structure in the elemental distribution. The width of the chromium bands are between 20 and 35 µm, and are probably formed during the rolling of the material. When comparing the chromium maps and manganese maps, it becomes visible that the banding of manganese is also present in the sample. While less pronounced, the manganese seems to follow the same structure as chromium. Where the concentration of chromium is increased due to the banding, the manganese concentration is also slightly increased. The width of the manganese bands, however, seems to be higher than chromium. Since manganese is more homogeneously distributed, the width of the bands is hard to determine.

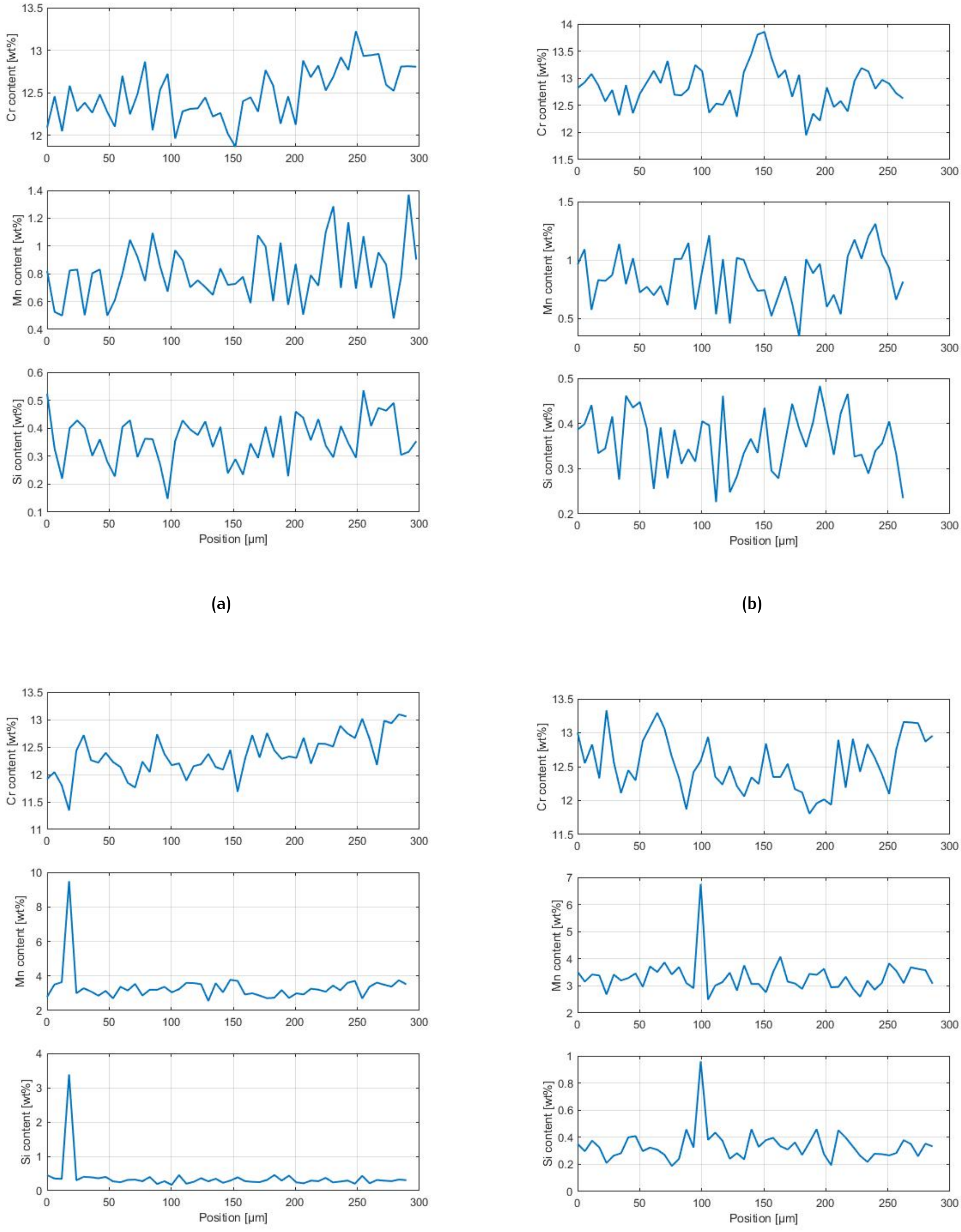

(a)

(b)

(c)

(d)

Figure 4.3: Quantitative linescan of elemental composition for (a) QP1, (b) QP2, (c) QP3 Mn and (d) QP4 Mn.

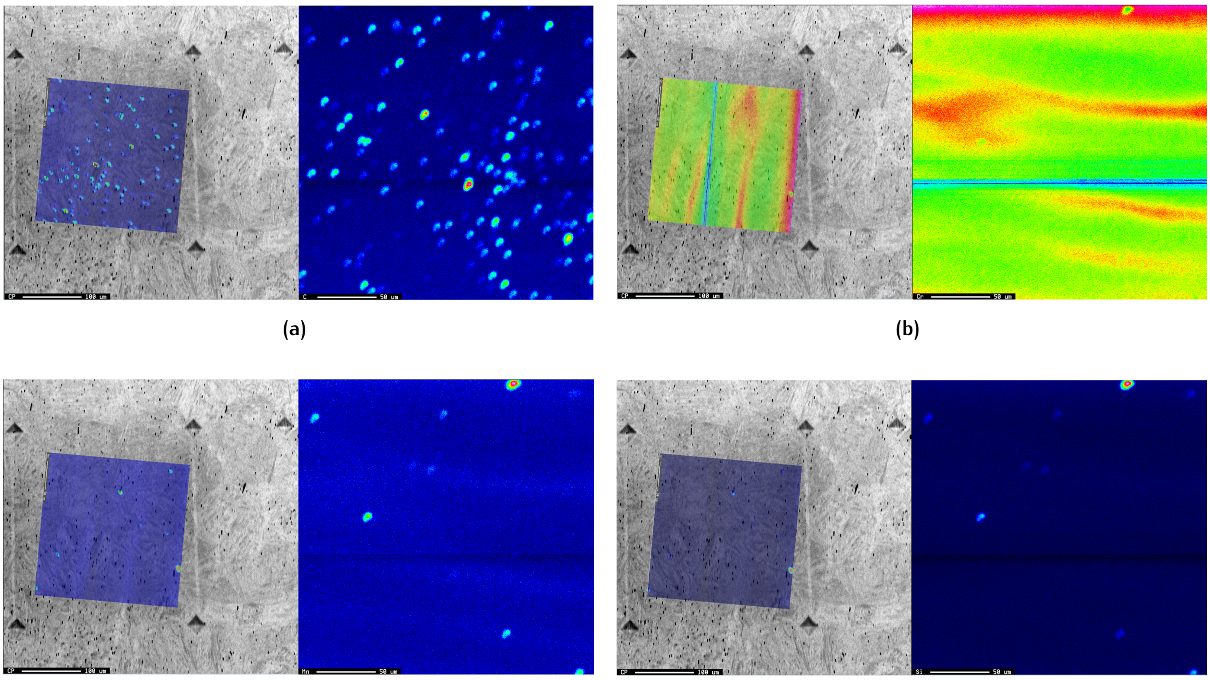

(a) (b)

(c) (d)

Figure 4.4: Qualitative elemental distribution maps acquired by EPMA analysis. (a) C content, (b) Cr content, (c) Mn content, (d) Si content of sample QP1. Scalebar of the micrographs are 100 µm, scalebar of the maps are 50 µm.

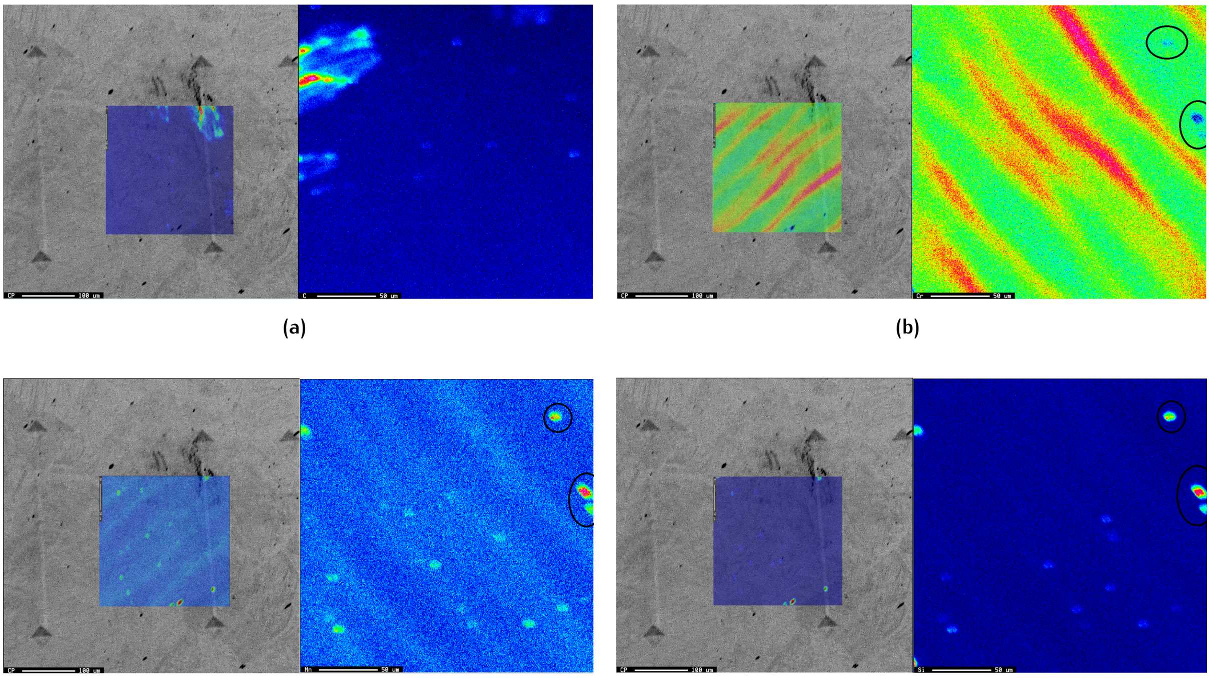

(a) (b)

(c) (d)

Figure 4.5: Qualitative elemental distribution maps acquired by EPMA analysis. (a) C content, (b) Cr content, (c) Mn content, (d) Si content of sample QP2. Scalebar of the micrographs are 100 µm, scalebar of the maps are 50 µm.

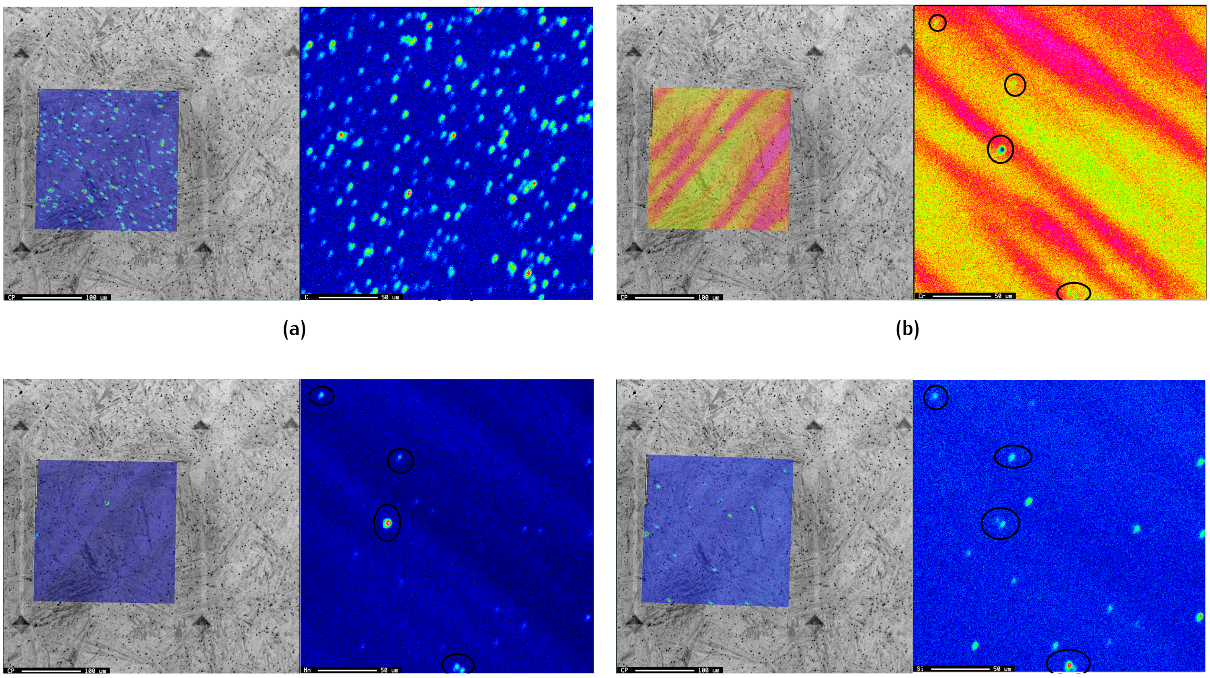

(a)

(b)

(c)

(d)

Figure 4.6: Qualitative elemental distribution maps acquired by EPMA analysis. (a) C content, (b) Cr content, (c) Mn content, (d) Si content of sample QP3 Mn. Scalebar of the micrographs are 100 µm, scalebar of the maps are 50 µm.

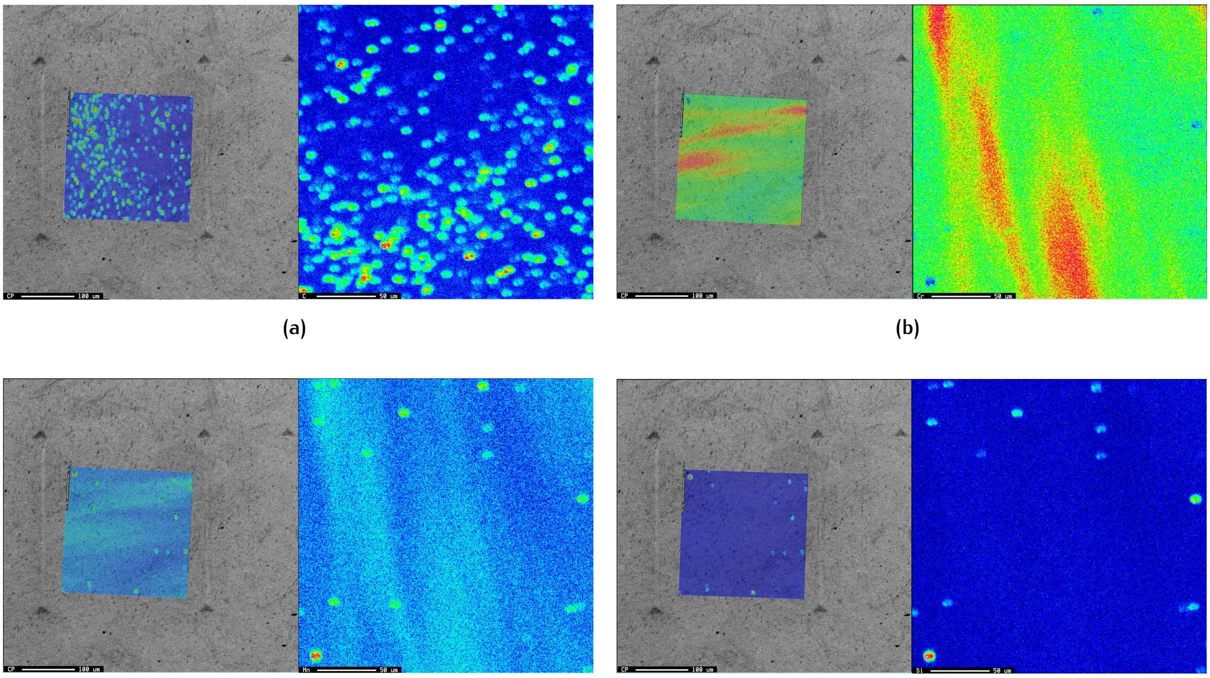

(a)

(b)

(c)

(d)

Figure 4.7: Qualitative elemental distribution maps acquired by EPMA analysis. (a) C content, (b) Cr content, (c) Mn content, (d) Si content of sample QP4 Mn. Scalebar of the micrographs are 100 µm, scalebar of the maps are 50 µm.

The elemental composition maps also show locally decreased concentrations of chromium. An example of these locations are shown by a black circle in Figure 4.5 and Figure 4.6, at these locations the concentration of chromium locally falls below the matrix concentration. When comparing these locations with the Mn and Si maps of both samples, it shows that at the same location the concentration of both Mn and Si is significantly increased. This indicates that locally certain precipitates are formed which decrease the local concentration of chromium. These precipitates are most probably the earlier mentioned manganese silicides. Because of the qualitative nature of these maps, an absolute value of the concentration of the elements can not be determined.

While the manganese silicides are observed in all sample, the higher manganese content of QP3 Mn and QP4 Mn could influence the formation of these particles in terms of particle number density. To analyze this, all maps were inspected in terms of amount of manganese, and silicon rich particles. Counting the number of Mn and Si rich particles per map, and dividing by the area of two maps (0.125 mm^2 total) gives the average particles per square millimeter. The results are given in Table 4.2. The results show that samples QP3 Mn and QP4 Mn have an increased amount of particles per unit area when compared to the low manganese sample QP1 and QP2.

Sample	Number of Mn and Si rich particles per mm^2
QP1	208
QP2	192
QP3 Mn	232
QP4 Mn	216

Table 4.2: Number of particles rich in manganese and silicon per square millimeter for each sample. Data extracted from EPMA maps.

All samples also show significant local increases in carbon concentration. While carbide precipitation is not allowed in the CCE model of quenching and partitioning, carbides are almost always observed in the final microstructure [9; 3; 11; 10]. Similarly for the steel used in this project, earlier research has shown that cementite like carbides observed in the microstructure [4]. It is therefore expected that the carbon concentrations shown in the EPMA maps also represent cementite (M_3C) like carbides.

Another interesting observation can be made when comparing the elemental distribution map of chromium, with micrographs of etched samples. Comparing the high-contrast image with the qualitative maps of Cr concentration, a clear overlap can be seen between the Cr bands and the blueish zones in the optical image. While it is difficult to determine if this dark band on the etched sample means the area is etched more, or to a lesser extent, it is interesting to observe that the chromium banding has a clear influence on the etching process. Since etching is a selective dissolution process, this indicates that the chromium banding can influence the speed at which different phases are being attacked by corrosion.

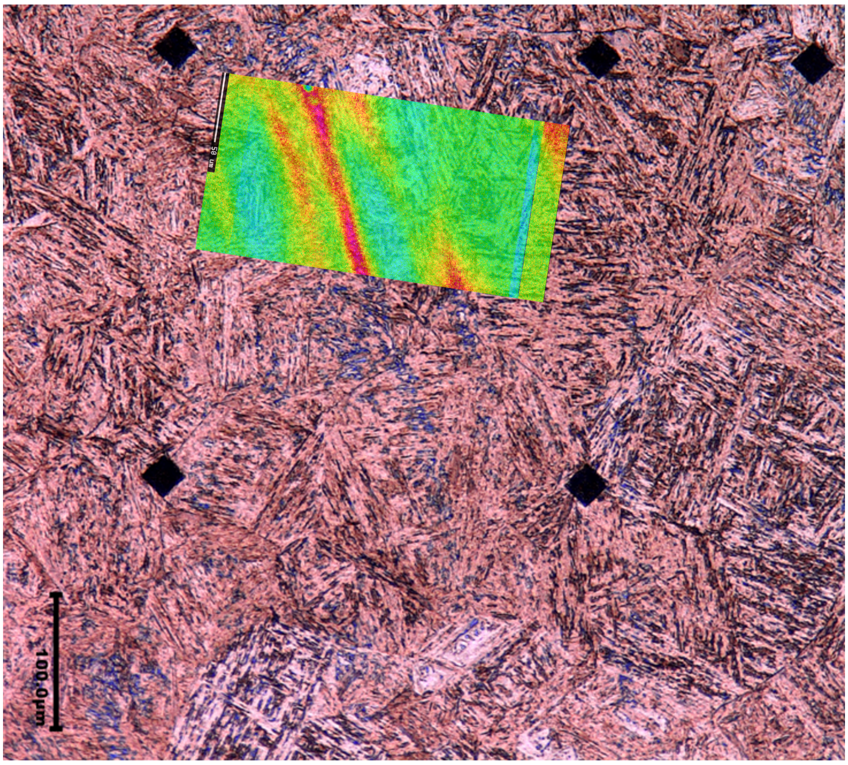

Figure 4.8: Overlap of EPMA Cr distribution map and high-contrast image of etched QP1.

4.1.3 Volta-potential Analysis by SKPFM

Scanning Kelvin Probe Force Microscopy (SKPFM) measures the Volta-potential differences of a sample down to micron level. SKPFM has been used to show the nobility of the sample surface, and see if microstructural features have influence on Volta-potential values.

Figure 4.9 shows the topography and Volta-potential maps of a square area scanned on one of the QP2 samples. The martensite structure clearly becomes visible with these scans. As preparation for the SKPFM scans the samples were polished with OPS for 15 minutes, causing slight selective etching of certain phases. Because of this, the topography map shows the martensite structure that is present in the sample, and a distinction between different martensite phases can be made. The first clear observation that can be made is that there are clear differences in topography for different blocks on the sample surface. One of these areas is marked with a white dashed line in Figure 4.9a. This area is less etched than the darker areas shown in the topography map. The reason for this is expected to be the difference between primary and fresh martensite. Fresh martensite is expected to be more cathodic, and will therefore be etched to a lesser extend. If we compare this area to roughly the same marked area in Figure 4.9b, it seems that this area also has a lower Volta potential. Again, because of the tip bias in this setup, a lower potential indicates more cathodic areas. This confirms that the marked area can indeed be fresh martensite. This can also be illustrated by a linescan over the full length of the scan to show the topography and the Volta-potential difference. These linescans are shown in Figure 4.9c, trendlines are added for easier visualization. In these linescans, once again, fluctuations of topography are visible. Low areas of topography coincide with higher Volta-potential values. This means that more etched areas of the sample have a more anodic Volta-potential. Figure 4.9c clearly shows that this trend fits for the complete length of the lines. Wherever the topography increases, the Volta-potential decreases.

The same observation can be made for a scan of sample QP4 Mn. This sample has a large fraction of fresh martensite, and can therefore show clear differences between the different martensite phases

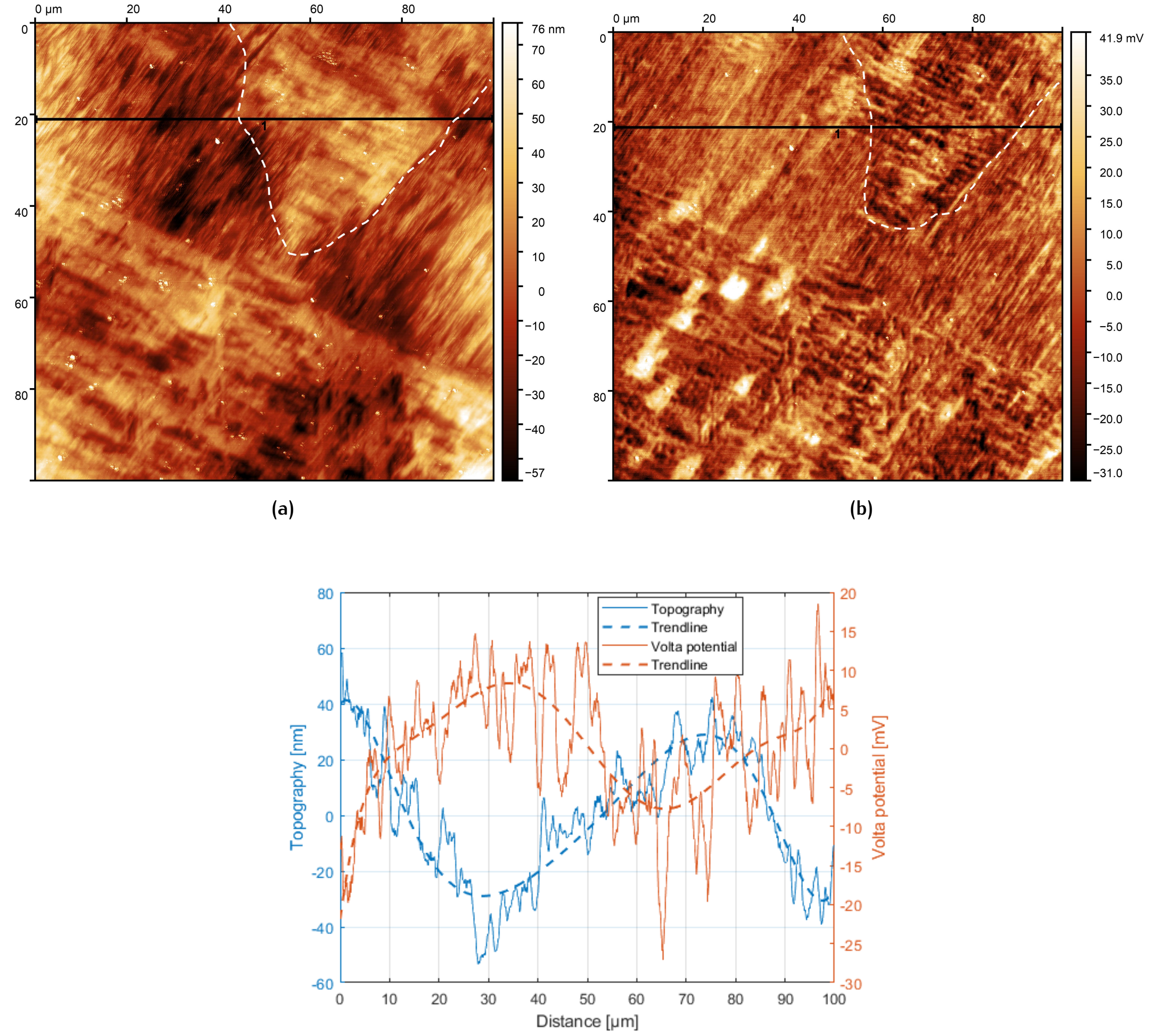

(a)

(b)

(c)

Figure 4.9: Topography map (a), Volta-potential (b) and extracted line data (c) for sample QP2.

as well. Figure 4.10 shows the topography map, Volta-potential map and linescan profiles of QP4 Mn. The topography differences in this sample are much bigger than for QP2, showing a clear difference between martensite phases, but no longer the lath structure. The linescan shows a relation between the topography and Volta-potential values, indicating the difference in martensite structure.

To quantify the difference in Volta-potential of different martensite phases more, the peaks of the Volta-potential data in the linescans was used to compare the phases. The resulting differences in Volta-potential for each martensite phase are shown in Figure 4.11. This plot clearly shows the difference in Volta-potential for primary (M1) and fresh (M2) martensite. While there is some overlap in Volta-potential, the values are significantly more positive for primary martensite, indicating more anodic behaviour.

A different scan of sample QP2 shows what seems to be a prior austenite grain boundary. Figure 4.12 shows an overlap of a topography map (orange) and a Volta-potential map (green) with the prior austenite grain boundary marked in white. While the Volta-potential map of this scan shows several high potential artifacts, an overlap of the topography and Volta-potential of the grain boundary

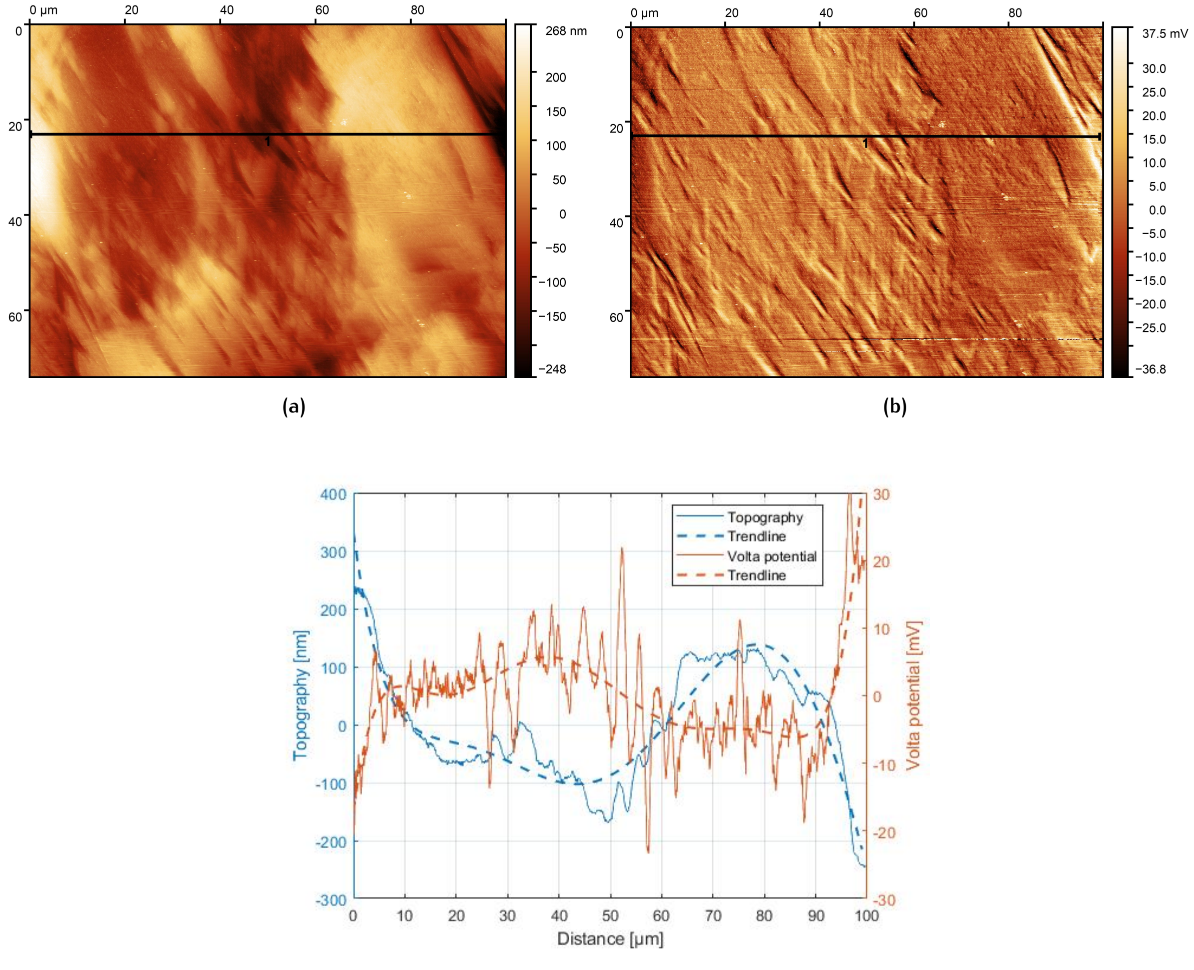

(a) (b)

(c)

Figure 4.10: Topography map (a), Volta-potential (b) and extracted line data (c) for sample QP4 Mn.

can be observed. This is an indication that microstrcutural features like grain boundaries can also have an influence on the Volta-potential of the surface.

As already mentioned before, in the scans of QP2, the shape of martensite laths becomes visible even in the Volta-potential maps. To investigate the influence of the laths on Volta-potential, more detailed linescans have been made on one map of QP2 and one map of QP4 Mn shown in Figure 4.13. The linescans show that there is a clear fluctuation in Volta-potential between martensite laths. Profile 1 in Figure 4.13d already shows an absolute difference of potential of about 50 mV. To visualize this potential difference further, the peaks (blue) and valleys (red) of the linescans across martensite laths are plotted as values per sample. These values are shown in Figure 4.14. This representation shows that there is a difference of Volta-potential between the martensite laths, much like shown earlier between different types of martensite. Interestingly, the difference between Volta-potential for QP4 Mn laths is bigger than the difference for QP2 laths.

Another detail highlighted in Figure 4.13a and Figure 4.13c is the presence of secondary phase particles with a high Volta-potential value. This value can spike up to 65-75 mV, and is significantly higher than the overall potential of the sample. The size of these particles seems to be in the range of several micrometers (4-6 micrometer), and again, due to tip bias show anodic behaviour in terms of the nobility of the material.

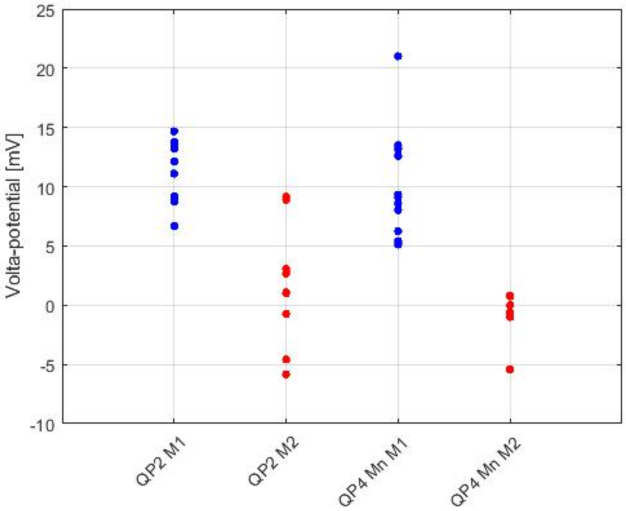

Figure 4.11: Difference in Volta-potential for M1 (primary martensite) represented in blue, and M2 (fresh martensite) represented in red for samples QP2 and QP4 Mn.

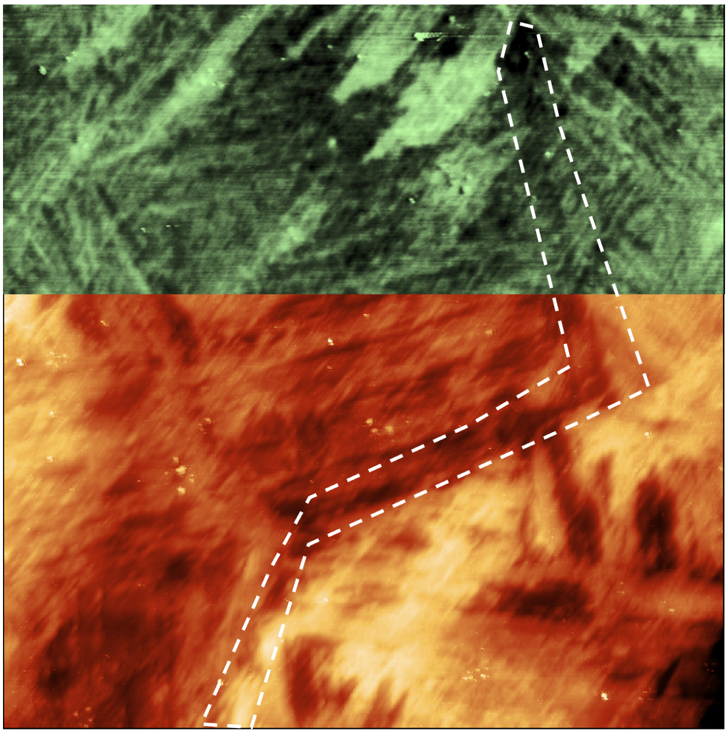

Figure 4.12: Prior austenite grain boundary on an overlap of topography (orange) and Volta-potential (green) of QP2. The size of the map is 100x100 µm

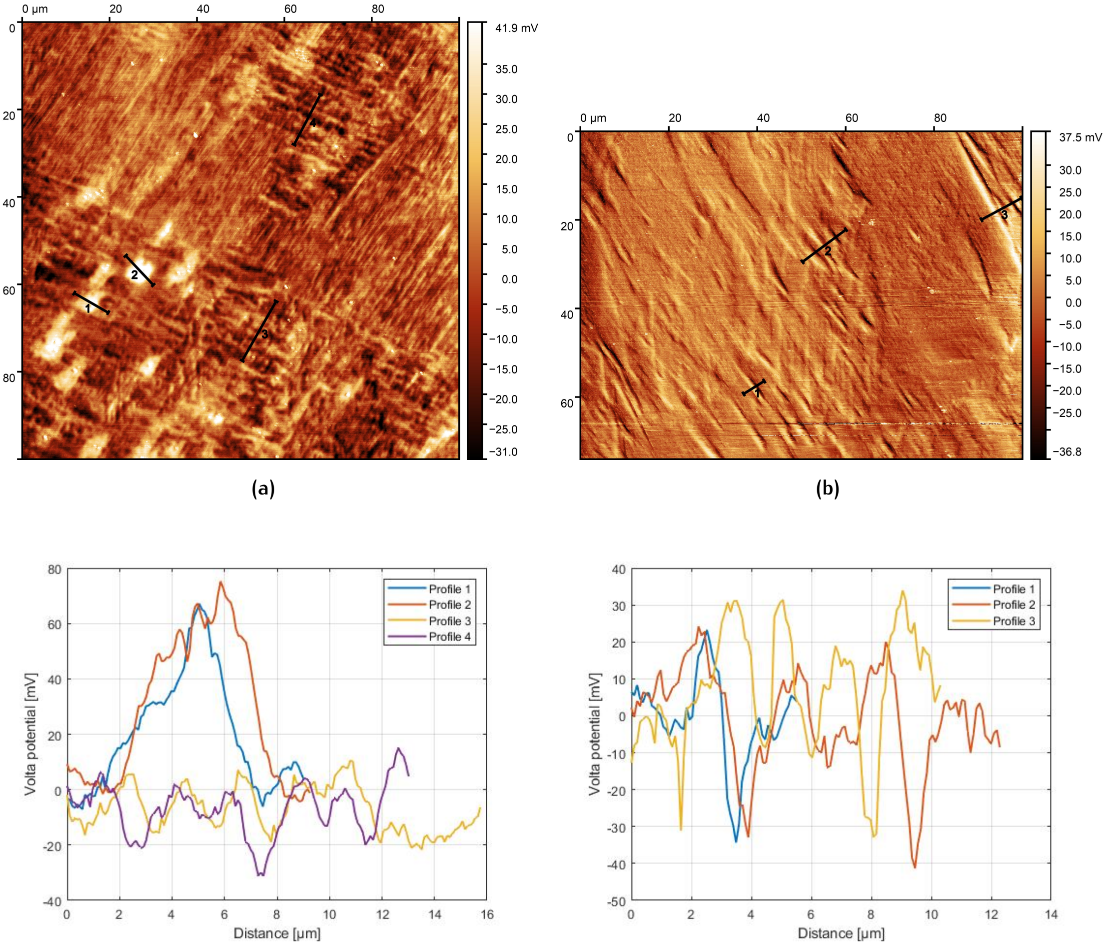

(a)

(b)

(c)

(d)

Figure 4.13: Volta potential maps of QP2 (a) and QP4 Mn (b), with linescans of different details (c) corresponds to QP2 and (d) corresponds to QP4 Mn.

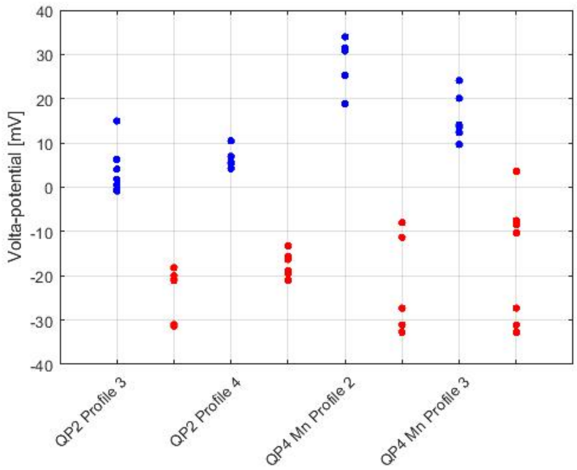

Figure 4.14: Potential difference between martensite laths for different linescans of samples QP2 and QP4 Mn. Blue represent the peaks in potential, red represents the valleys in potential.

4.2 ELECTROCHEMICAL CHARACTERISATION

First of all an overview of the Open Circuit Potential (OCP) will be given for each set of samples. Then the Potentiodynamic Polarization plots will be shown for all samples, and all additional information that can be concluded from these plots. This will be followed by the results of Electrochemical Impedance Spectroscopy (EIS). Both the Nyquist and Bode plots will be shown. This chapter will be closed by showing some optical micrographs of corroded samples.

4.2.1 Open Circuit Potential

The open circuit potential is primarily used as input for the electrochemical impedance spectroscopy and potentiodynamic polarization. These methods require a potential as a reference point. But the OCP can also give information about other aspects of the corrosion behaviour of the material. The OCP values for AISI 420 was measured for one hour, but the OCP measurements for the QP samples was extended to 1.5 hours to ensure a stable value

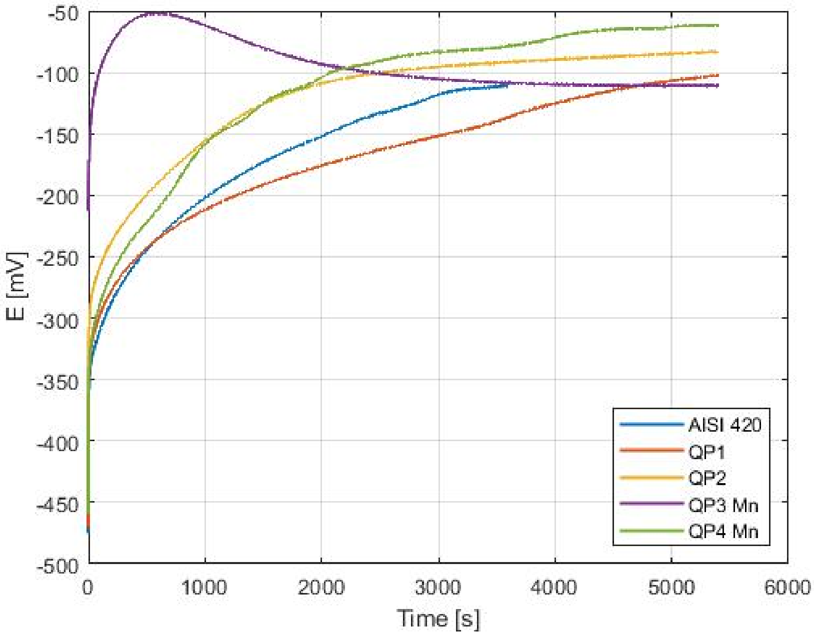

Figure 4.15: Open circuit potential measurements for commercial AISI 420 and the Quenched and Partitioned samples in 3.5 wt% NaCl.

The figure shows that all samples have a potential that steadily increases with time. Since the cathodic polarization method was used to strip the samples of the initial passive layer, the OCP shows the formation of the new passive layer on the steel. The interesting observation that can be made here, is that for all samples, except QP3 Mn, the OCP value steadily increases and eventually becomes relatively constant. The QP3 Mn sample, however, shows a much steeper increase in potential in the first seconds of the measurement. After this steep increase, the value reaches a maximum and then decreases to a relatively constant value. This occurrence was only consistently present in the QP3 Mn sample. It could indicate that the QP3 Mn sample initially forms a more noble passive layer, but this layer is not completely stable. After some time, the layer develops to its stable state and decreases in terms of potential.

The results shown in Figure 4.15 show a single repetition of each sample. It is, however, important to consider that a single repetition for the OCP value will not give a good indication of the general behaviour of the sample that is being considered. Therefore, for each sample, the OCP measurement has been performed at least four times. For sample QP4 Mn the results were consistent enough to only require three repetitions. Figure 4.16 represents the average OCP values with error margins. The average of the OCP was taken from the last five minutes of measuring.

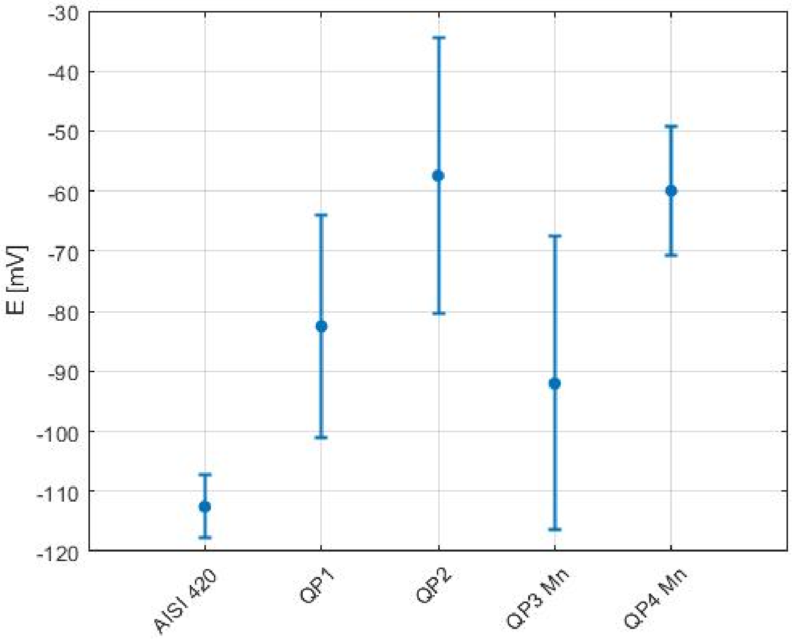

Figure 4.16: Average open circuit potential (taken over last 5 min) and error margin for commercial AISI 420 and the Quenched and Partitioned samples in 3.5 wt% NaCl.

The averages show that there is an increase in potential for the Q&P treated samples compared to the AISI 420 sample. There seems to also be an increase in potential between QP1 and QP2. However, the error margins in these measurements is significant. So while there is a difference of approximately 20 mV between the averages of QP1 and QP2, the error margins indicate that, in reality, the OCP values of both samples can be close to each other for specific repetitions. Especially comparing QP1 and QP3 Mn, these samples can be considered as having generally the same OCP values. When adding manganese to the composition, there seems to be a significant drop in OCP value. Comparing QP2 and QP3 Mn, these samples have very similar phase fractions, as seen in Table 4.1, but the OCP drops by approximately 30 mV for the average value. QP4 Mn then once again shows an increase in OCP value equal to QP2.

4.2.2 Potentiodynamic Polarization

Potentiodynamic polarization is a useful technique to gain insight into the kinetics of the corrosion process and pitting behaviour of the samples. The potentiodynamic polarization plots are shown in Figure 4.17. All samples show immediate passivation, as would be expected of martensitic stainless steel in 3.5 wt% NaCl. After the passive region, at high potentials, the samples show breakdown due to pitting. The current density increases drastically, indicating that the passive film has failed, and a corrosion pit has been formed on the exposed surface. For AISI 420, QP1 and QP2, the passive region shows a very stable current density. The samples containing manganese, however, show transients in the current density, indicating the presence of metastable pitting during the scan. Metastable pitting is an occurrence that happens when the passive film locally breaks down, but immediately repassivates.

Several important parameters can be obtained from the potentiodynamic polarization curves. Corrosion current density (I_{corr}), corrosion potential (E_{corr}), passive current density (I_{pass}) and pitting potential (E_{pit}) can all be used to evaluate the corrosion performance of the different samples, the

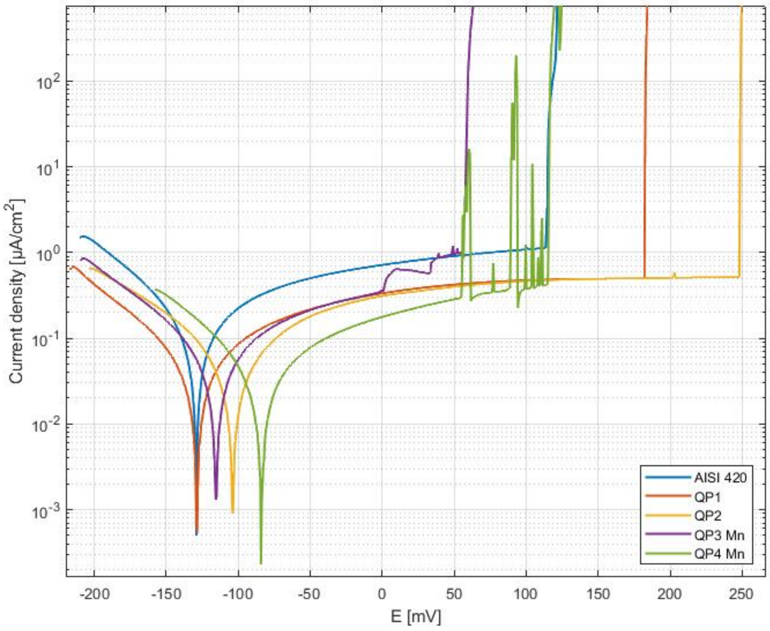

Figure 4.17: Potentiodynamic polarization plots for commercial AISI 420 and the Quenched and Partitioned samples in 3.5 wt% NaCl.

values for these parameters are given in Table 4.3. Firstly, the corrosion current density for all samples are very low, as expected for martensitic stainless steel. The corrosion current density is acquired by Tafel extrapolation. Comparing these corrosion current densities can be useful to rank the samples in terms of corrosion performance. The corrosion current density for AISI 420 is slightly higher then for the Q&P treated samples, this is to be expected since the chemical composition of both materials is not exactly the same. For the Q&P samples, all corrosion current densities relatively fall in the same range. This observation can also be made for the passive current density. Again, the value for the AISI 420 is slightly higher, showing the difference in composition.

Sample	$I_{corr} * 10^{-8} [A/cm^2]$	$E_{corr} [mV]$	$I_{pass} * 10^{-7} [A/cm^2]$	$E_{pit} [mV]$
AISI 420	5.05 ± 1.3	-125 ± 6	6.25 ± 2	127 ± 19
QP1	2.38 ± 0.8	-107 ± 19	4.05 ± 1.6	187 ± 70
QP2	3.50 ± 0.2	-75 ± 28	4.83 ± 0.5	223 ± 35
QP3 Mn	2.25 ± 0.4	-111 ± 16	3.52 ± 0.7	57 ± 19
QP4 Mn	2.20 ± 0.3	-67 ± 22	4.00 ± 0.9	118 ± 11

Table 4.3: Corrosion current density (I_{corr}), corrosion potential (E_{corr}), passive current density (I_{pass}) and pitting potential (E_{pit}) of AISI 420 and quenched an partitioned samples in 3.5 wt% NaCl.

To visualize the passive region better, the values for the length of the passive region (E_{pit}-E_{corr}) have been plotted in a separate graph. Figure 4.18 shows the length of the passive region with error margins of the pitting potential for each sampel. Samples QP1 and QP2 show a slight increase in passive region compared to AISI 420. When manganese is added, the pitting potential and length of passive regions decrease drastically. QP3 Mn and QP4 Mn both show a very low length of passive region compared to the other two QP treated samples, and even lower than AISI 420. QP4 Mn, however, shows a slight increase in the passive region when compared to QP3 Mn.

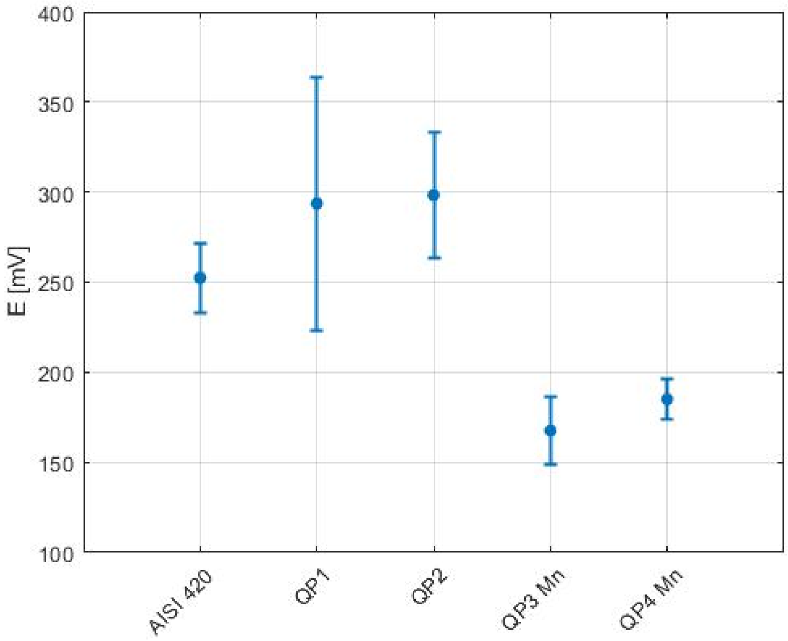

Figure 4.18: Comparison of the length of the passive region for all samples (E_{pit}-E_{corr}).

4.2.3 Electrochemical Impedance Spectroscopy

Electrochemical Impedance Spectroscopy (EIS) uses an alternating potential on the sample surface, the impedance (Z) can then be measured and is used to analyze different properties of the electrolyte/metal interface. Impedance can be seen as the tendency of a system to impede the flow of this alternating potential. The results of this technique will be presented in the form of Nyquist and Bode plots for the samples.

Figure 4.19 shows the Nyquist plots for all samples. At first, the arc radii seem to indicate that the passive film properties of QP1 are best, followed by QP3 Mn. Both QP2 and QP4 Mn just barely have a bigger arc radii than AISI 420. Figure 4.20 and Figure 4.21 show the Bode plot, and phase angles of all samples, respectively. For all the Nyquist and Bode plots, a single repetition is shown as a representation of the data obtained.

To gain quantitative information from the EIS data, fitting with an equivalent electrical circuit was done. While the circuit in Figure 4.22a is a very common circuit to fit the EIS data in stainless steel research, and was also used by Lu et al.[3] it was found that this circuit was not able to fit the data correctly. The parameters of fitting would not follow both the Nyquist and Bode curves simultaneously. While the data does not immediately suggest the presence of a second time constant (the phase angle plots give some indication for QP2 and QP3 Mn), the circuit presented in Figure 4.22b showed a much better fit for the EIS data (see Appendix A for a comparison of data fitting with both circuits). This circuit is also often used in the literature for stainless steel and passive materials with oxide layers [32; 33; 34; 35]. In this circuit R_s represents the resistance of the electrolyte, CPE_{dl} and R_{ct} represent the constant phase element of the double-layer and resistance of charge transfer, respectively. CPE_{ox} and R_{ox} are added in this circuit to represent the capacitance and resistance of the passive layer, respectively [34; 35]. The resulting fitting parameters for the data can be seen in Table 4.4.

More information about the passive layer formed on the sample can be obtained with the CPE_{ox} parameters α and Q_o, and the resistance of the passive layer R_{ox}. The capacitance value C can be determined by the following equation [36]:

$$C_{film} = R^{\frac{1-\alpha}{\alpha}} Q^{\frac{1}{\alpha}} \tag{4.1}$$

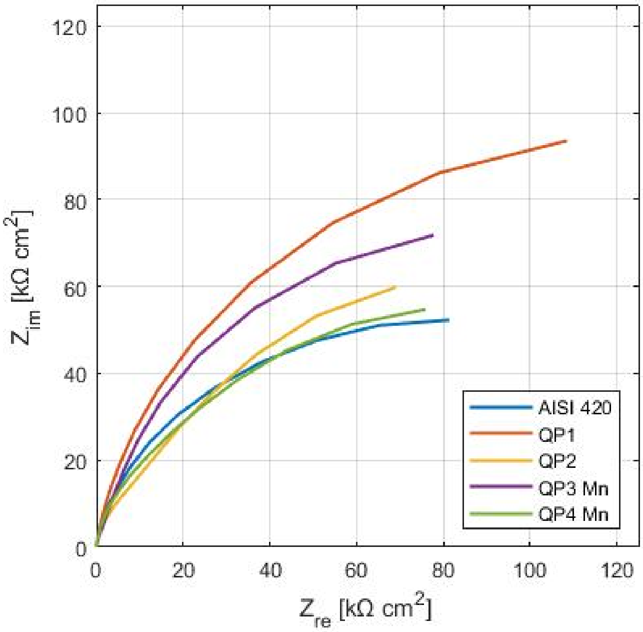

Figure 4.19: Nyquist plots for commercial AISI 420 and the Quenched and Partitioned samples in 3.5 wt% NaCl.

Where R respresents the resistance element and Q and α the CPE parameters. Using this capacitance, the thickness of the passive film on the samples can be calculated by the follwing equation [35]:

$$\delta = \epsilon \epsilon_0 A / C_{film} \tag{4.2}$$

Where δ is the thickness of the passive film, ϵ the relative dielectric constant, ϵ_0 the vacuum dielectric permittivity (8.84 pF/m), A the capacitor surface area and C_{film} the calculated capacitance from Equa-

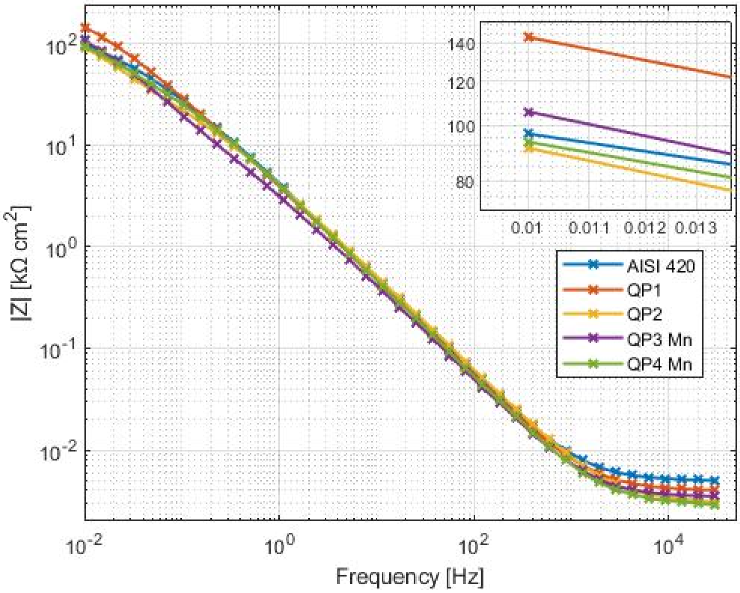

Figure 4.20: Bode plots for commercial AISI 420 and the Quenched and Partitioned samples in 3.5 wt% NaCl.

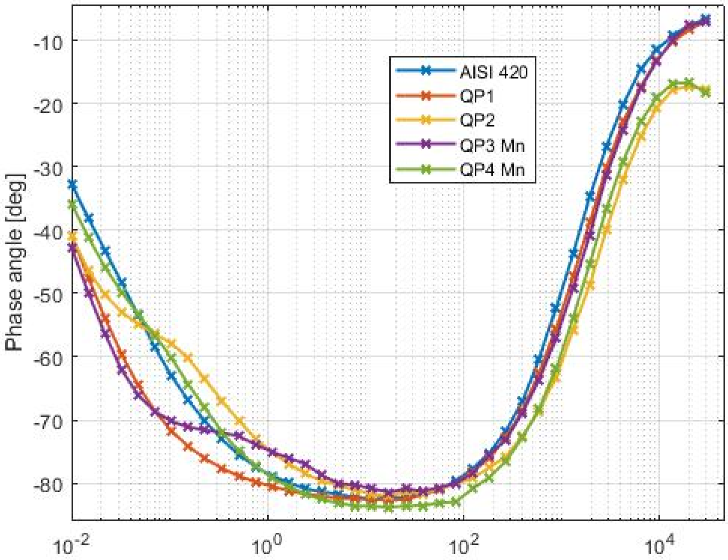

Figure 4.21: Phase angles for commercial AISI 420 and the Quenched and Partitioned samples in 3.5 wt% NaCl.

tion 4.1. ϵ in this case is taken as 15.6 for martensitic stainless steel [37]. The calculated capacitance values, and resulting passive layer thickness are shown in Table 4.5

The fitting parameters are overall in agreement with the bode plots. QP1 and QP3 Mn show the highest resistance to corrosion due to high passive layer resistance values (R_{ox}), followed by AISI 420. QP2 and QP4 Mn are flipped with respect to the impedance values of the Bode plot. This can be explained due to the fact that the fitting parameters show averages of the data of all repetitions of each sample. The Bode plots of Figure 4.20 show the repetition that was closest to the average impedance value of all repetitions. Since there is often scatter in these values, the representation of the Bode plot can be slightly misleading compared to the fitting parameters.

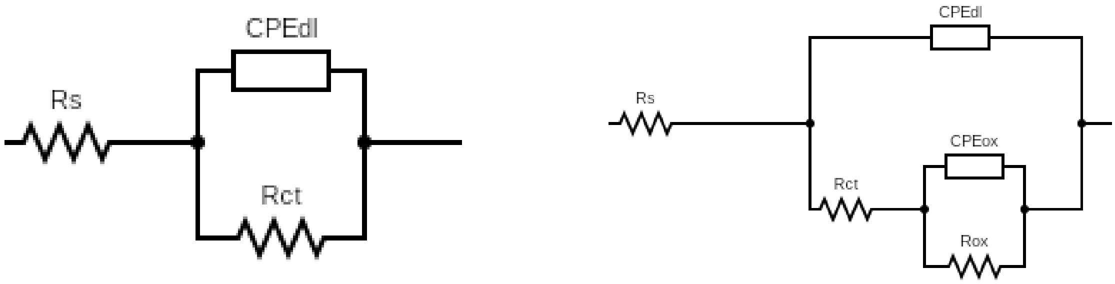

(a)

(b)

Figure 4.22: Equivalent circuit used for EIS data fitting in [3] (a), equivalent circuit proposed for the data of this thesis (b)

Sample	$R_s [\Omega cm^2]$	CPE_{dl}		$R_{ct} [k\Omega cm^2]$	CPE_{ox}		$R_{ox} [k\Omega cm^2]$	$\chi^2 * 10^{-3}$
		α	$Q_0 [\mu S cm^{-2} s^n]$		α	$Q_0 [\mu S cm^{-2} s^n]$		
AISI 420	4.20 ± 1.2	0.91 ± 0.04	52.62 ± 14.3	24.38 ± 18.5	0.49 ± 0.04	43.65 ± 21.7	133.33 ± 18.2	1.62 ± 0.9
QP1	3.27 ± 0.7	0.88 ± 0.06	55.63 ± 10.4	59.06 ± 22.4	0.67 ± 0.17	22.03 ± 16.1	235.02 ± 47.5	5.52 ± 3.7
QP2	2.84 ± 0.6	0.92 ± 0.03	42.95 ± 2.7	45.97 ± 25.6	0.74 ± 0.05	53.88 ± 17	119.38 ± 32.4	3.44 ± 1.9
QP3 Mn	3.62 ± 0.4	0.92 ± 0.01	48.22 ± 6.4	23.03 ± 8.8	0.70 ± 0.09	28.46 ± 8	181.78 ± 23.6	2.23 ± 1.5
QP4 Mn	3.61 ± 0.9	0.93 ± 0.02	48.42 ± 4.1	61.42 ± 22.8	0.79 ± 0.03	61.97 ± 35.6	112.75 ± 30.3	4.54 ± 1.5

Table 4.4: Fitting parameters of the EIS data for different samples.

Sample	C_{film} $[\mu F/cm^2]$	δ [nm]
AISI 420	272.97	0.05
QP1	49.52	0.28
QP2	103.62	0.13
QP3 Mn	57.56	0.24
QP4 Mn	103.90	0.13

Table 4.5: Capacitance values C_{film} calculated from Equation 4.1 and passive film thickness δ calculated from Equation 4.2.

4.2.4 Optical Micrographs after Corrosion

Another use of optical microscopy is to investigate the samples after they have been corroded due to the electrochemical experiments. After the potentiodynamic polarization, pits have been formed on the surface which can be shown with optical micrographs.

Figure 4.23 shows a selection of micrographs of corroded samples. Figure 4.23a and Figure 4.23b show micrographs of pit formation on a QP1 sample. For this sample, the central pit seems to have grown, surrounded by several other smaller pits. Overall, the pit size of all samples is comparable and falls in a range of 150-200 µm. Most samples show the formation of several small pits, which eventually coalesce to form larger pits. This is best visible in Figure 4.23h, in this image the smaller pits are eventually connected and will form large pits if corrosion would be allowed to continue.

Besides the pits, another interesting observation can be made from the corroded samples. Figure 4.24 shows corrosion on a much smaller scale than pitting for sample QP3 Mn and QP4 Mn. These micrographs show the dissolution of selective phases. The selective dissolution in Figure 4.24a seems to happen in needle-like shapes. Which could indicate that specific martensite phases are being attacked by corrosion before other phases are attacked. Besides the selective dissolution in martensite shaped features, Figure 4.24b also shows corrosion in the shape of grain boundaries. This occurrence of selective corrosion was present for all samples and seemed to be unrelated to the different amount of phase fractions, or the difference in manganese content.

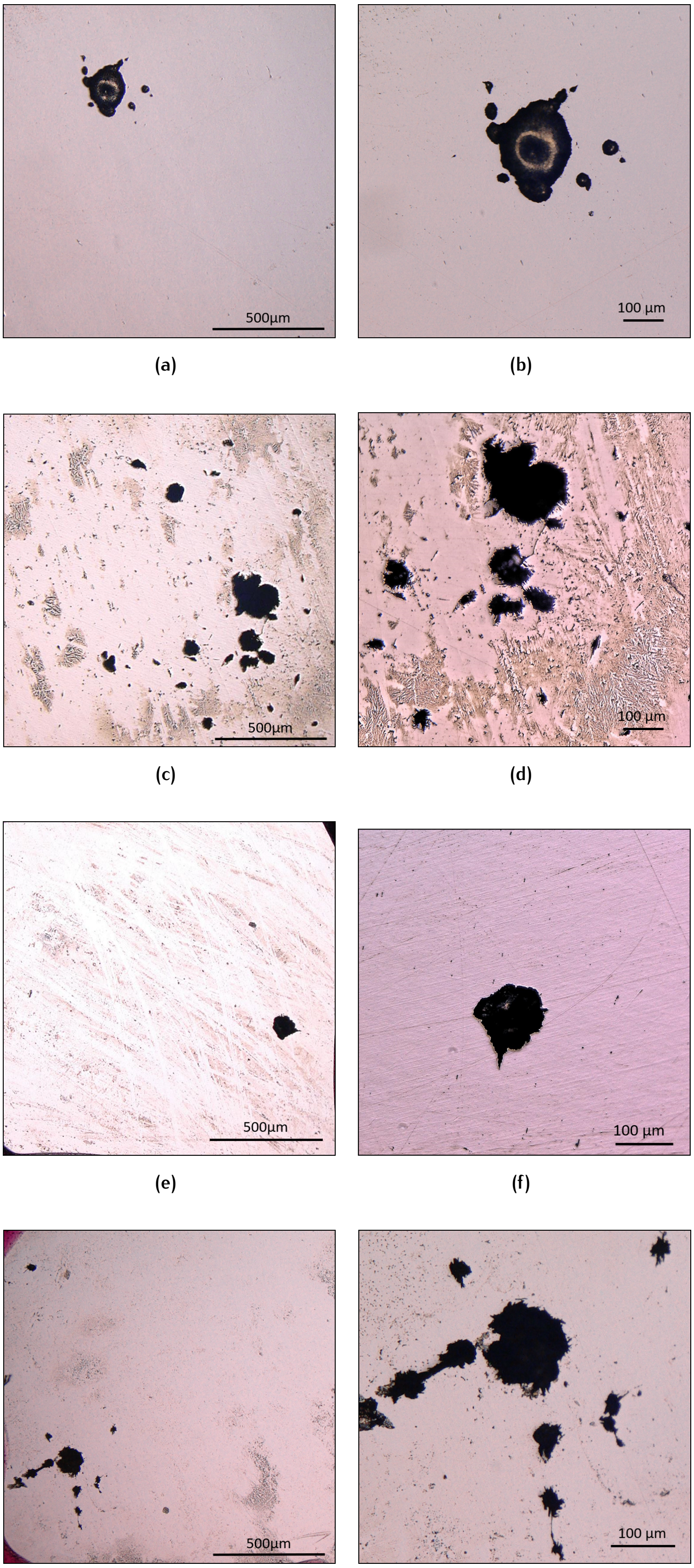

(a) (b)

(c) (d)

(e) (f)

(g) (h)

Figure 4.23: Selected micrographs showing the samples after the polarization experiments. (a) and (b) are sample QP1, (c) and (d) QP3 Mn and (e) and (f) show sample QP4 Mn.

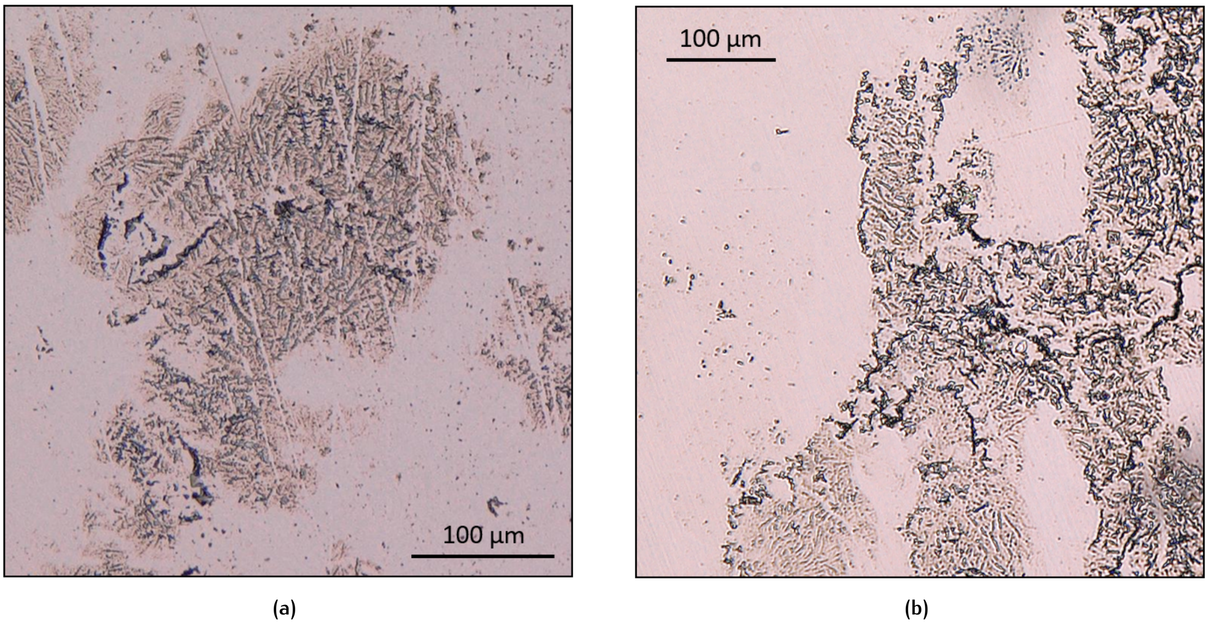

Figure 4.24: Selective dissolution of phases on sample QP3 Mn (a) and QP4 Mn (b).

5 DISCUSSION

This chapter will discuss the results presented in Chapter 4, with the aim to relate these results to the research objectives proposed in the Introduction.

5.1 THE CORROSION PERFORMANCE OF AISI 420 VS. Q&P TREATED MARTENSITIC STAINLESS STEEL

Chapter 4 mainly showed the corrosion performance of both AISI 420 commercial stainless steel, and the novel Q&P treated martensitic stainless steel. The results of this chapter can be used to critically evaluate the corrosion properties of AISI 420 compared to Q&P treated martensitic stainless steel.

Figure 4.16 shows the average OCP values of all samples. This figure makes it clear that the AISI 420 steel exhibits the lowest OCP value (and therefore also the lowest E_{corr} value) of all samples. This indicates that in the same environment, the AISI 420 sample will act more anodic than the Q&P samples. The parameters that are extracted from the potentiodynamic polarization plots in Figure 4.17 show similar behaviour when compared to the OCP values. In Table 4.3, the I_{corr} and I_{pass} values both are significantly higher than for the Q&P samples. The AISI 420 sample, therefore, shows the worst corrosion performance of all samples in the same environment.

The pitting potentials, however, show a different situation. To compare the pitting potential in a more accurate way, the length of the passive region is plotted in Figure 4.18. This figure shows that the low manganese Q&P samples have a better pitting performance. While there is some overlap in the error margin of QP1, on average this sample still shows a higher passive region when compared to AISI 420. The AISI 420 sample in its as-received state is annealed. During annealing, carbide precipitation will be expected similar, or even to a larger extend, to the carbide formation during tempering. This means that in the AISI 420 samples, $M_{23}C_6$ or M_7C_3 carbides which are rich in chromium can be expected [38]. These carbides have a detrimental effect on the pitting performance of the sample [3; 19; 20]. The improved performance in the case of samples QP1 and QP2 can then be attributed to the fact that these chromium-rich carbides are not expected in the microstructure after Q&P treatment. Almost in all research done in the microstructural evolution of Q&P treated MSS, only cementite like θ-M_3C precipitated, which are expected to not reduce the surrounding chromium content in the matrix [9; 3; 11; 10]. Only in samples with very low silicon contents were M_7C_3 observed [11], which is not the case in this research. As shown in the EPMA elemental distribution maps, spikes the in concentration of carbon are present in the samples. This is expected to be due to carbide formation in the form of cementite like particles similar to previous research [4]. This, together with the fact that the austenitization temperature and Q&P parameters were chosen to prevent chromium-rich carbides from forming, indicates that these carbides will most probably not form chromium depleted zones. This is also confirmed when comparing the carbon elemental distribution maps with the chromium maps of the Q&P samples, as shown in Figure 4.4 - Figure 4.7. The high carbon concentration, and thus carbides, do not overlap with the chromium depleted zones observed in the samples. However, the samples with high manganese content show a severe drop in terms of pitting potential and length of the passive region as seen in Figure 4.18. There is a clear influence of manganese on the pitting of the samples. This will be discussed further in the following section.

The results from the EIS measurements are generally in agreement with the results from potentiodynamic polarization. At first, the resistance of the oxide layer for AISI 420 is lower than at least QP1 and QP3 Mn as shown in Table 4.4. The resistance of the QP2 and QP4 Mn samples are slightly lower than AISI 420, but the α value is much lower for AISI 420. Low α values are generally an indication of a less homogeneous passive layer, indicating that while the resistance is higher, the passive layer is not as homogeneous as for the Q&P samples. [39].

As can be seen from the results of film thickness for each sample, the thickness of the passive film (Table 4.5 on AISI 420 is much smaller than the Q&P samples. The values of the passive film thickness of the Q&P samples seem to be slightly smaller than would be expected at the austenitization temperature of 1150°C as shown in research by Bösing et al. [39], and are in good agreement with the results of Lu et al.[3]. Bösing et al. [39] showed that the austenitization temperature has a great influence on passive film growth. It can therefore be expected that there will be differences in passive film development for different heat treatments, explaining the large difference between AISI 420 and Q&P samples. The combination of thinner passive layer, and less homogeneous layer as shown by the α parameter confirms the observations from the potentiodynamic polarization plots in terms of lower I_{pass}, pitting potential and higher I_{corr} values. It has to be noted that the resulting film thicknesses shown in Table 4.5 is semi-quantitative, as it is based on the capacitance value of the EIS data. More exact analysis of the passive film could be done by XPS or Mott-Schottky analysis.

Overall, the corrosion performance of AISI 420 compared to Q&P treated martensitic stainless steel is worse (with the exception of the samples where manganese is added). The most important factor in this drop in performance is most probably the formation of chromium-rich carbides which decrease passive film properties, and form locations susceptible to localized attacks by pitting corrosion. The annealed material is expected to form these chromium-rich carbides much like, tempered martensitic stainless steel. The literature in tempering and annealing agrees with these observations that the carbides are dominating in the corrosion performance [38]. What should also be taken into consideration is the fact that the AISI 420 sample has double the carbon content compared to the Q&P material. This will most probably also have an effect on carbide formation, and therefore corrosion properties.

5.2 CORROSION PROPERTIES OF QUENCHED AND PARTITIONED MARTENSITIC STAINLESS STEEL

As shown in Chapter 3, this thesis investigated the corrosion properties of four samples treated with different quenching temperatures. This results in different phase fractions which can be seen in Table 4.1. In addition to the phase fractions, two samples had higher manganese content in the composition. The influence of different phases and manganese will be discussed in the following subsections.

5.2.1 Influence of Retained Austenite on corrosion properties

As before, the first indication in to the corrosion properties of the samples can be seen in the OCP values shown in Figure 4.16. There is an increase of 25 mV in terms of average OCP value between QP1 and QP2. Table 4.1 showed that the retained austenite fraction in QP2 increased to 20.8% from 11.1% for QP1. This increase in OCP value can, therefore, be caused by the increase in austenite. The austenite is saturated with carbon in order to stabilize. This is the integral goal of the quenching and partitioning treatment. This higher fraction of retained austenite with high carbon content will, therefore, become a more cathodic phase compared to martensite and will increase the OCP value of the material. It is important, however, to mention that the error margins cause overlap in the OCP values of QP1 and QP2. While there is a clear increase in average OCP value, Figure 4.16 also shows that there are repetitions that can be overlapping.

The passive current densities of both samples seem to be in the same range, indicating no impact of the increased retained austenite. The corrosion current density of Table 4.3 shows a higher current density for QP2. Indicating that while the sample might act more cathodic in terms of E_{corr} and OCP value, the corrosion rate is actually slightly increased. The reason for this could be that increased fractions of retained austenite can lead to the formation of galvanic cells. Volta-potential measurements were done to see if the formation of micro-galvanic cells is possible. All the Volta-potential maps shown in Chapter 3 (Figure 4.9, Figure 4.10 and Figure 4.13) show that there are differences between microstructural features. The differences in Volta-potential for sample QP2 (Figure 4.9) are approximately 40 mV. This could indicate that there is a potential difference between phases. However, Volta-potential maps have been known to be affected by differences in height [31], to avoid this, careful sample preparation has been taken into consideration. Samples have been polished with OP-S (0.25 µm) to avoid the influence of height on the sample surface. Therefore, since the differences in Volta-potential generally follow the topography maps, the fluctuations in potential are expected to be differences in martensite laths. Due to the fact that the retained austenite grains are so small, their potentials get washed out by the differences between martensite laths. In any case, a distinction of the retained austenite grains in the Volta-potential maps is not easily done.

The influence of retained austenite on the corrosion current density is also questioned by sample QP3 Mn. While an increase in retained austenite fraction from sample QP1 to QP2 indicates an increase in corrosion current density, sample QP3 Mn has the highest fraction retained austenite at 25%. This sample, however, shows corrosion current densities in the same range as sample QP1. This could, however, also be influenced by manganese. The influence of manganese will be discussed in a later subsection.

Sample QP2 also has a significantly higher pitting potential when compared to QP1 (Table 4.3). This increase in pitting potential can mainly be attributed to the shift of the corrosion potential. As discussed previously, the OCP value and, therefore, the corrosion potential, is increased in QP2 most probably due to the presence of more retained austenite which will cause the material to act more cathodic. It is, therefore, important to compare the samples in terms of the length of the passive region, in other words; E_{pit}-E_{corr}. This length of the passive region is shown in Figure 4.18. This figure indicates that the length of the passive region for both samples is actually almost equal. So while the material has a more cathodic E_{corr}, the potential range before pitting occurs is similar in both samples, indicating comparable corrosion performances in terms of pitting. For this case, comparison with sample QP3 Mn is not applicable. While this sample has the highest austenite phase, the addition of Mn seems to have a significant effect on localized corrosion performance, hindering the effect of retained austenite.

The EIS data also seems to be inconclusive on the question of wether the addition of retained austenite improves corrosion performance. Sample QP2 shows a thinner passive film than QP1 (Table 4.5). However, the thickness of the passive film is not always an indication of better passive film properties [39]. The α parameter of the CPE of the oxide layer in Table 4.4 suggests that while the passive film for QP1 is thicker, the passive film of sample QP2 is more homogeneous. When taking these factors into consideration, the passive film of QP2 seems to be significantly more homogeneous, and therefore have better corrosion properties. However, values of the oxide layer resistance in Table 4.4 indicate that the oxide resistance is higher in sample QP1 compared to QP2.

Overall, the effect of retained austenite on the corrosion performance of Q&P treated martensitic stainless steel does not become immediately clear from the presented results. While the OCP or E_{corr} values increase with increasing retained austenite fraction, the pitting potential (more precisely, the length of the passive region) and EIS data do not reflect the increase in corrosion performance. This is mostly in line with what Lu et al.[3] also found in their research. While an increase in pitting potential was observed (they did not consider comparing the pitting potential in terms of passive region length), this was not directly linearly related to increased austenite fractions. The sample with the highest retained austenite fraction barely performed better than tempered samples. They did show that there was a difference in the shape of retained austenite. When the austenite was in film or needle-like shape, the pitting potential increased. When the retained austenite was in larger block shapes, the pitting potential was only marginally increased. The shape and distribution of austenite could, therefore, must have a larger influence on corrosion properties than the actual phase fraction. It could very well be that more distributed and film shaped retained austenite can improve corrosion performance by relieving internal stresses of the martensite as argued by Yang et al.[28].

5.2.2 Influence manganese on corrosion properties

In the previous subsection it was discussed that the addition of retained austenite mainly increases the OCP or E_{corr} values, and therefore shift the pitting potential to higher values. If we consider the length of the passive region and the EIS data, there does not seem to be a relation between retained austenite and increased corrosion resistance, though. With this knowledge, a good comparison between sample QP2 and QP3 Mn can be made to investigate the effect of manganese on the corrosion performance of quenched and partitioned martensitic stainless steel. These two samples were shown in Table 4.1 to have very similar phase fractions, with approximately a 4.2% difference in retained austenite. This difference in retained austenite can now be expected to barely impact the corrosion properties between the samples. Therefore, the main difference is the manganese content of 0.7wt% in sample QP2, and 3wt% in sample QP3 Mn. The other chemical components are equal for both samples as shown in Table 3.1.

Once again, the OCP and E_{corr} values can be considered first. There seems to be an immediate drop of 30-35 mV in terms of average OCP and average E_{corr} values when higher manganese contents are added. Between samples QP1 and QP2, the rise in these parameters is expected to be due to the higher retained austenite fractions. However, these samples have similar phase fractions, so the drop in potential can be attributed to the addition of manganese. Samples QP1 and QP2 also showed different OCP and E_{corr} values, but the corrosion properties based on pitting potentials and EIS data did not explicitly show an increase. Again, it must be noted that while a significant difference in average OCP values is observed, the error margins cause overlap between these sample much like the comparison of QP1 and QP2. For the comparison between QP2 and QP3 Mn, however, there is a clear drop in both pitting potential, and length of the passive region. The values of E_{pit} in Table 4.3 and the values of the length of passive region in Figure 4.18 clearly show that when manganese is added, the sample is much more susceptible to pitting corrosion.

Comparing the EIS data for these samples, Figure 4.19 and Figure 4.20 both show that the passive film properties of QP3 Mn are superior to the properties of QP2. The fitting parameters indicate that the film thickness (Table 4.5) of QP3 Mn is almost twice as big as QP2. Also, the oxide resistance (R_{ox}) is higher for the QP3 Mn sample when compared to QP2. However, the slightly lower α parameter in Table 4.4 for QP3 Mn also indicates that the passive film on this sample is less homogeneous than for sample QP2. This can be the crucial difference for pitting to occur. Imperfections in the passive layer will be preferential pitting sites. These imperfections can be in the form of carbides or other secondary phase particles.

The EPMA results presented in Chapter 4 can give an interesting insight into the decreased corrosion performance of the high manganese samples. As shown in Figure 4.4 - Figure 4.7, there are clear indications of decreased chromium content, compared to the surrounding matrix. These decreases in chromium content can be detrimental to the resistance against pitting corrosion, since these areas of low chromium content will decrease passive film properties locally. This is much like the influence of chromium-rich carbides in quenched and tempered stainless steels. This is further confirmed by the quantitative linescans performed by EDS in Figure 4.3. The linescans for both high manganese samples show the presence of manganese silicides. It can be observed that these manganese silicides often overlap with the locally decreased chromium concentrations. Considering the quantification of these particles in Table 4.2, it is clear that the samples with high manganese have a larger number of these manganese silicides per unit area. The trend of the number of particles per unit area actually is in very close agreement with the lengths of passive regions in Figure 4.18. Sample QP3 Mn and QP4 Mn have 232 and 216 particles per mm^2, respectively. Samples QP1 and QP2 show 208 and 192 particles per mm², respectively. There is a connection between the number of particles per unit area, and the pitting behaviour of the samples. The length of passive region is also slightly higher for QP4 Mn than for QP3 Mn, which is supported by the number of particles per mm² as well. Previous research in pitting corrosion in 316L stainless steel by Laleh et al. [40] also showed the presence of these manganese silicides. They found that in addition to manganese and silicon, the particles also show increased oxygen concentration. This could indicate the particles are $MnSiO_3$. Unfortunately, for this research oxygen content was not investigated by EDS/EPMA. The size of the precipitates is difficult to determine from the qualitative EPMA maps. While they give an indication, a halo of concentration gradient is visible, making the determination of absolute size impossible. Also, due to the larger step size (6 µm) for the EDS measurements, the size determination is not possible from these linescans. An estimation of size from the EPMA maps show that the size of the precipitates is between 2-10 µm. In the research of Laleh et al. [40], they also observed the depletion of chromium at the particle locations, as well as the particles being in micron range and having a spherical shape, much in line with the presented results.

Another reason for the manganese rich particles can be the formation of manganese-sulfide (MnS) inclusions. MnS has been observed in steels with Mn contents lower than 1wt% [21], and can, therefore, very well form in both alloys. While the chemical compositions of the stainless steel used in this thesis do not contain any sulfur, it is still an impurity element present in stainless steel at 0.03wt%, and formation of MnS inclusions is possible [41]. MnS inclusions have been shown to be preferential pitting sites by reducing the matrix chromium composition [21], which is in line with the EPMA results.

The evaluation of Volta-potential of the samples by SKPFM seem to agree with the EPMA results. Figure 4.9 and Figure 4.13 show areas with spikes in Volta-potential. As discussed in Chapter 3, more positive Volta-potentials indicate that the area is more anodic, which is the opposite of the normal electrochemical convention, where positive potentials normally indicate more cathodic. This is due to the applied bias of the SKPFM, which in this thesis was applied to the tip. From the extracted profile data, these precipitates have an increased Volta-potential difference of between 65-80 mV. Earlier research on MnS inclusions with SKPFM showed that these inclusions act more anodic than the surrounding matrix [42], showing that the particles observed can indeed be MnS inclusions. The manganese silicides in stainless steel are much less documented in the literature. At the time of reading, no information about Volta-potential measurements of manganese silicides in stainless steel was available. Manganese silicide has been reported as behaving more anodic with respect to the matrix for aluminium alloys [43]. However, since aluminium and stainless steel are vastly different materials, the assumption that manganese silicides will also behave anodic in a stainless steel matrix can not directly be made.

Overall the observation can be made that addition of manganese greatly decreases the corrosion performance of the Q&P samples. The increased number of particles formed per unit area due to the high manganese content (manganese silicide or MnS) are easy locations for localized corrosion. Besides the formation of chromium depleted zones and, therefore, weak spots in the passive film formation, the Volta-potential of these samples shows anodic behaviour compared to the matrix. This could potentially form micro-galvanic cells, also decreasing corrosion performance.

5.2.3 Influence of fresh martensite

Earlier, the comparison was made between sample QP2 and QP3 Mn to show the difference in corrosion properties caused by addition the of manganese. This comparison could be done since the phase fractions of both samples were very similar. To compare the influence of fresh martensite on corrosion properties, sample QP3 Mn and QP4 Mn can be compared. This time the manganese content is equal again (3wt%), but sample QP4 Mn has a very large amount of fresh martensite (48.6%).

The high fraction of fresh martensite results in a significant rise of the OCP and E_{corr} values (Figure 4.16 and Table 4.3), causing the sample to act more cathodic. This is most probably for a similar reason than the increase in retained austenite, the fresh martensite is supersaturated with carbon and will act more cathodic. While there is a significant increase in pure pitting potential, the length of the passive region is actually only marginally increased as seen in Figure 4.18. Considering the error margins on the pitting potentials, the difference between length of the passive regions for sample QP3 Mn and QP4 Mn could be considered negligible. In any case, fresh martensite is considered to be undesirable in general for the quenching and partitioning treatment. The aim is to achieve a microstructure consisting of very specific fractions of primary martensite and retained austenite. The very small improvement in terms of length of passive region therefore would not warrant the use of higher fresh martensite fractions to prevent pitting corrosion. The EIS data indicates that the passive film properties are worse for QP4 Mn than the properties of QP3 Mn. Figure 4.19 show much smaller arc radii, and the fitting parameters confirm this observation. Table 4.5 shows that the passive film thickness of QP 4 Mn is only half the thickness of QP3 Mn (again, the passive film values are only semi-quantitative). There does seem to be an increase in α, indicating a more homogeneous passive film. The oxide resistance for QP4 Mn are also show lower resistance values when compared to QP3 Mn, agreeing with the arc radii in the Nyquist plots.

QP4 Mn can also be compared to QP1. This time the samples have similar fractions of retained austenite (11.1% for QP1 and 8.3% for QP4 Mn), but vastly different fractions of fresh martensite (4.2% for QP1 and 48.6% for QP4 Mn) and different manganese content. As discussed before, the manganese content plays a big role in the localized corrosion performance of the samples. This heavily influences pitting potentials. Therefore, EIS data will be considered to compare the passivity of these samples. The comparison between these samples is similar to the comparison between QP3 Mn and QP4 Mn. Once again, QP4 Mn, with its high fraction of fresh martensite, shows a passive film thickness of only half that of the QP1 sample. The α parameter does show that the passive film on QP4 Mn is slightly more homogeneous. The oxide resistance also shows similar trends. The oxide resistance for QP4 Mn is significantly lower than the oxide resistance of QP1, showing easier charge transfer through the oxide film. Since this trend is similar to the comparison with QP3 Mn, the conclusion can be drawn that high fractions of fresh martensite have negative influences on the passivity of the samples.

The SKPFM results nicely show the difference between different martensite phases. As mentioned before, fresh martensite will have a higher carbon content when compared to primary martensite, and will be more cathodic due to this carbon. When polishing with OPS (which also etches the sample slightly) the phases will, therefore, be dissolved at different rates. Figure 4.9 and Figure 4.10 clearly show large blocks which have differences in topography. In Figure 4.9 a less etched grain is marked in white, indicating the presence of fresh martensite. The Volta-potential signals generally overlap with these regions of different topography. Where the topography is higher, and fresh martensite is expected, the Volta-potential signals are more negative, indicating cathodic behaviour. This relation can be seen in both linescans of Figure 4.9c and Figure 4.10c. This shows that there are clear Volta-potential differences between primary and fresh martensite. This is shown in more detail in Figure 4.11, the plot shows a difference of, on average, 10 mV for the different martensite phases, and differences between extreme values of more than 20 mV. This potential difference can be an indication that primary and fresh martensite phases can cause micro-galvanic cells. It then becomes clear that QP4 Mn, containing more fresh martensite, shows worse corrosion properties in general.

5.2.4 Influence of elemental banding on corrosion performance

The EPMA results presented in Chapter 4 showed clear banding of different elements in the microstructure. Especially banding of chromium could have an impact on corrosion properties. If the difference between the high regions and low regions of the chromium bands are large enough, the uniformity of the passive film could be impacted. In the results, it was calculated and shown by EDS that this fluctuation can be as high as 1.5wt%, which is in line with previous research [4]. Since the banding is expected to influence the passivity of the material more than the localized corrosion like pitting, the EIS data could indicate difference due to banding. This banding is present, however, in all samples. There seems to be no clear difference in number of bands, or band width between different samples. As all samples come from the same base material, and the banding structure is a result from the rolling of this base material, it is expected that the banding for the samples will be similar. No clear relation between the EIS data, and the particular banding per sample can be shown. This indicates that the banding has very low influence on the passivity of the samples.

However, in previous research on the microstructural development of this particular martensitic stainless steel during quenching and partitioning, it was shown that the elemental distribution of chromium and manganese does have an effect on the local phases that are formed. The banding of both elements affects the martensite start temperature, influencing the formation of local phases. Low chromium and manganese regions showed a higher martensite start temperature, resulting in higher fractions of primary martensite in these regions [4]. The discussion about the influence of fresh martensite in the previous subsection already showed that the different martensite phases can influence corrosion performance. So while no direct relation between elemental banding and passivity properties can be found, an indirect influence of elemental banding on corrosion properties due to phase formation is possible.

While there are no immediate observations of chromium banding impacting the corrosion properties, Figure 4.8 did show that the banding can be visible by optical microscopy during etching. This does show that banding has effect on etching. However, etching is very different from the corrosion of stainless steel in, for example, NaCl conditions. The influence of banding is, therefore, expected to be of little significance on the corrosion properties of Q&P treated MSS, even while visible by etching.

5.2.5 Influence of other microstructural features

As discussed before, the corrosion properties of quenched and tempered martensitic stainless steel are dominated by chromium-rich carbides that precipitate during the tempering treatment. While these are generally not observed during quenching and partitioning, θ-M_3C carbides are most definitely observed in quenched and partitioned martensitic stainless steel [9; 3; 11; 10]. In the EPMA maps of carbon, clear spikes in concentration were observed, indicating the presence of carbides. Based on previous research, these are expected to be cementite-like carbides[4]. Carbides in the matrix would in theory be a cathodic particle, since it has high concentrations of carbon. The presence of carbides could, therefore, be shown by SKPFM Volta-potential maps. There are spikes in topography maps shown in Figure 4.9 which indicate particles that are harder when compared to the matrix, and less etched. Carbides have been shown in the research by Hayakawa et al.[44] to indeed show high topography features when the samples are etched. However, none of the observed spikes in topography actually show a low Volta-potential signal (cathodic), indicating they could be carbides. Most of the spikes in topography actually show anodic behaviour, showing the presence of manganese silicide or MnS inclusions. So, while carbides are definitely present in the microstructure, there is no clear Volta-potential difference with the matrix. The carbides could still be preferential pitting initiation sites as they can be considered imperfections in the matrix. However, since the carbides are present in all samples, they are not expected to influence the corrosion properties when comparing the Q&P treated samples.

Another interesting observation made by the SKPFM measurements was the presence of a prior austenite grain boundary. Figure 4.12 shows an overlay of the topography and Volta-potential map, with the prior austenite grain boundary indicated with a dashed line. There is a clear difference of topography on either side of the prior austenite grain boundary, indicating that different martensite phases can have formed. However, the Volta-potential map also shows a region of low Volta-potential exactly on the prior austenite grain boundary. Low Volta-potentials indicate a more cathodic behaviour. Prior austenite grains and their size have been shown to clearly impact the formation kinetics of phases in medium carbon steel during quenching and partitioning [6]. This, together with the difference in Volta-potential, can indicate that the prior austenite grains could also have a significant impact on the corrosion properties of quenched and partitioned martensitic stainless steel. The current results, however, can only show a possible influence, and does not show the exact relation between these factors.

The last microstructural influence that could play a role in corrosion of quenched and partitioned martensitic stainless steel, is the formation of micro-galvanic corrosion cells between different phases. As already discussed in the previous subsection, this can occur between primary and fresh martensite. However, as shown in Figure 4.13, Volta-potential fluctuations between martensite laths are clearly visible. Figure 4.14 better visualizes the different Volta-potentials between the martensite laths. Fluctuations of approximately 40 mV in sample QP2 and 70 mV QP4 Mn can be observed. These fluctuations indicate that there can be different behaviour in terms of nobility between martensite laths. This could cause the formation of micro-galvanic cells, much like primary and fresh martensite as discussed before. This observation is actually in line with the observations of corroded samples in Figure 4.24. In these micrographs, clear selective dissolutioning is observed in what seems to be needle-like shapes. This can be an indication that the difference in Volta-potential between laths can indeed influence corrosion.

6 CONCLUSION

6.1 CONCLUSIONS

This thesis investigated the influence of several microstructural features on the corrosion properties of novel quenched and partitioned stainless steel. Two alloys with chemical composition 0.2C-12.5Cr-0.35Si-XMn, where X will be 0.7 for the low manganese alloy, and 3 for high manganese alloy, were considered for this study. Samples of the alloys were first characterized by optical microscopy combined with etching, Electron Probe Microanalysis (EPMA), Energy Dispersive Spectroscopy (EDS) and Scanning Kelvin Probe Force Microscopy. This was combined with electrochemical characterisation by Open Circuit Potential (OCP) measurements, potentiodynamic polarization and Electrochemical Impedance Spectroscopy (EIS). The research objective, results and discussion led to mainly the following conclusions:

- The novel quenched and partitioned martensitic stainless steel showed significant improvement in terms of corrosion properties compared to AISI 420 commercial stainless steel. The main factor in this difference will be chromium-rich carbides that have formed in the AISI 420 sample. The carbides form chromium depleted zones which act as preferential initiation sites for pitting. While the Q&P treated samples do form carbides in the microstructure, these are expected to be cementite-like carbides that are not rich in chromium. The high manganese Q&P treated samples form an exception. These samples show even worse performance against localized corrosion due to the high manganese content.

- Increasing fractions of retained austenite can not directly be related to an increase in corrosion properties. While an increase in E_{corr} is observed due to a larger fraction of carbon-rich phase, the length of the passive region (E_{pit}-E_{corr}) does not increase significantly. EIS data also does not seem to support an increase in corrosion properties. The shape and distribution of retained austenite could, however, be a larger factor in increasing corrosion properties.

- Fresh martensite largely has a similar influence on corrosion properties compared to retained austenite. The E_{corr} values have increased, but the length of the passive region generally showed small improvement. However, the EIS data suggests that an increase in the fraction of fresh martensite has a significant impact on the passivity of the material. Both the passive film thickness, and the oxide resistance decrease with increasing fractions of fresh martensite. SKPFM results clearly show both differences in topography and Volta-potential signals. The high topography regions are expected to be fresh martensite as they will have been etched less. The Volta-potential map then shows that there are clear differences between the primary martensite and fresh martensite, with fresh martensite being more cathodic and primary martensite acting more anodic, indicating potential formation of galvanic cells.

- Addition of manganese severely increases the tendency for pitting in the quenched and partitioned martensitic stainless steel. EPMA elemental distribution maps show several locations with increased manganese content and locations depleted of chromium. A combination of the EDS and EPMA results indicate that manganese silicide, or manganese sulfide inclusions are present in the material. While these inclusions are present in all samples, the high manganese samples have an increased number of particles per unit area, causing worse localized corrosion performance. The SKPFM results show anodic particles present in the matrix, which are in line with the expected manganese silicides or manganese sulfides.

- No clear relation between the elemental banding of chromium, found by EPMA analysis, and the passivity properties of the samples can be observed from the EIS data. However, during etching, a clear overlap between chromium bands and darker etched bands are present. So while the chromium banding does have an influence on etching, the extend of this influence on the passivity is not clear
- SKPFM results have shown that a prior austenite grain boundary has an influence on the Volta-potential measurement. While no clear relation between prior austenite grains and corrosion properties can be concluded from these results, there are influences on local potential values.
- Optical micrographs after corrosion show clear selective dissolution of phases. This, together with the Volta-potential fluctuations between presumably martensite laths, indicate the formation of micro-galvanic cells. These fluctuations seem to increase in samples with higher fresh martensite fractions, indicating bigger potential differences between martensite laths.

Overall, this thesis shows that the microstructure of martensitic stainless steel has a large influence on the corrosion properties of the material. The largest changes in the corrosion performance seem to be caused due to the formation of secondary phase particles like carbides, or manganese rich inclusions. Advanced characterization techniques are necessary to not only discover the presence of these particles, but also show their impact on corrosion properties.

6.2 FUTURE RECOMMENDATIONS

The findings in this thesis warrant the following recommendations for further research:

- First of all, the differences in phase fractions can more closely be researched by considering more samples. In this research, the influence of phases was often determined by comparing two samples with different phase fraction. However, using, for example, five different samples with different fractions of retained austenite, or fresh martensite can give more insight into the influence of these phase fractions. These different phase fraction can easily be achieved by changing the quenching temperature in the Q&P treatment, as shown in [4]
- To more accurately analyse the influence of the increased manganese and decreased chromium concentrations, the precipitates have to be further analyzed. The EPMA elemental distribution maps can not determine the exact chemical structure of these particles. While they are expected to be manganese silicides or MnS in this thesis, more in-depth characterization is needed.
- SKPFM measurements in this thesis were done in atmospheric conditions. To gain more insight in the direct potential differences of the microstructure, SKPFM measurements could be done which more closely resemble the electrolyte conditions. While fully immersing the material in electrolyte is not possible for SKPFM, atmospheres can be humidified by passing air through NaCl solutions. However, the question then arises if this can correctly simulate real immersion in electrolyte.
- Highly localized electrochemical techniques can distinguish precipitated or other microstructural feature in terms of corrosion properties. Microcapillary techniques can be used to show the different behaviour of, for example, the local high manganese and low chromium zones after proper characterisation.
- Prior austenite grains are clearly visible in the presented micrographs. Grain size has been shown to greatly influence corrosion properties. This, together with the fact that the literature has shown that the prior austenite grain size also influences phase formation of Q&P steels [4; 6], and influences the Volta-potential measurements, indicates that this parameter will also influence corrosion properties. Samples with different prior austenite grain sizes could be investigated to show the impact on corrosion properties.

- To more accurately characterize the passive film, more specialized techniques like XPS or Mott-Schotkky measurements can be done. EIS does provide information about the passivity of the material, but the calculations of the passive film thickness are only semi-quantitative.

BIBLIOGRAPHY

[1] D.K. Matlock and J.G. Speer. Third generation of AHSS: microstructure design concepts. In *Microstructure and texture in steels*, pages 185–205. Springer, 2008.

[2] J.G. Speer, F.C. Rizzo Assunção, D.K. Matlock, and D.V. Edmonds. The "quenching and partitioning" process: background and recent progress. *Materials Research*, 8 (4):417–423, 2005.

[3] S. Lu, K. Yao, Y. Chen, M. Wang, N. Chen, and X. Ge. Effect of quenching and partitioning on the microstructure evolution and electrochemical properties of a martensitic stainless steel. *Corrosion Science*, 103:95–104, 2016.

[4] B. de Bakker. Influence of quenching temperature and Mn content on the microstructure development of new Q&P processed martensitic stainless steel. *Delft University of Technology*, 2021.

[5] N. Baluch, Z. M. Udin, and C.S. Abdullah. Advanced high strength steel in auto industry: an overview. *Engineering, Technology & Applied Science Research*, 4 (4):686–689, 2014.

[6] C. Celada-Casero, C. Kwakernaak, J. Sietsma, and M.J. Santofimia. The influence of the austenite grain size on the microstructural development during quenching and partitioning processing of a low-carbon steel. *Materials and Design*, 178:107847, 2019.

[7] M.J. Santofimia, L. Zhao, R. Petrov, and J. Sietsma. Characterization of the microstructure obtained by the quenching and partitioning process in a low-carbon steel. *Materials Characterization*, 59 (12):1758–1764, 2008.

[8] J.G. Speer, D.K. Matlock, B.C. De Cooman, and J.G. Schroth. Carbon partitioning into austenite after martensite transformation. *Acta Materialia*, 51 (9):2611–2622, 2003.

[9] J. Mola and B.C. De Cooman. Quenching and partitioning (Q&P) processing of martensitic stainless steels. *Metallurgical and Marterials Transactions A*, 44 (2):946–967, 2012.

[10] T. Tsuchiyama, J. Tobata, T. Tao, N. Nakada, and S. Takaki. Quenching and partitioning treatment of a low-carbon martensitic stainless steel. *Materials Science and Engineering: A*, 532:585–592, 2012.

[11] J. Tobota, K. Ngo-Huynh, N. Nakada, T. Tsuchiyama, and S. Takaki. Role of silicon in quenching and partitioning treatment of low-carbon martensitic stainless steel. *ISIJ International*, 52 (7):1377–1382, 2012.

[12] RINA-CSM., Acerinos Europa., IMDEA Materials Institute., and Delft University of Technology. Development of New Martensitic Stainless Steel for Automotive Lightweight Structural Applications (QPINOX). *https://www.qpinox.eu/*.

[13] M. Hillert and J. Årgen. On the definitions of paraequilibrium and orthoequilibrium. *Scripta Materialia*, 50 (5):697–699, 2004.

[14] M. Hillert and J. Årgen. Reply to comments on "On the definition of paraequilibrium and orthoequilibrium". *Scripta Materialia*, 52 (1):87–88, 2005.

[15] H. Bhadeshia and R. Honeycombe. *Steels: Microstructure and Properties*. Butterworth-Heinemann, 2017.

[16] L. Wang and J.G. Speer. Quenching and partitioning steel heat treatment. *Metallography, Microstructure, and Analysis*, 2 (4):268–281, 2013.

[17] M.J. Santofimia, L. Zhao, and J. Sietsma. Overview of mechanisms involved during the quenching and partitioning process in steels. *Metallurgical and Materials Transactions A*, 42 (12):3620–3626, 2011.

[18] K. Godbole, Panigrahi B.B., and Das. C. Tailoring of mechanical properties of AISI 410 martensitic stainless steel through tempering. *Proceedings 26th International Conference on Metallurgy and Materials*, pages 705–710, 2018.

[19] S.K. Bonagani, V. Bathula, and V. Kain. Influence of tempering treatment on microstructure and pitting corrosion of 13 wt.% Cr martensitic stainless steel. *Corrosion Science*, 131:340–354, 2018.

[20] G. Chakraborty, C.R. Das, S.K. Albert, V. Thomas Paul, Panneerselvam G., and A. Dasgupta. Study on tempering behaviour of AISI 410 stainless steel. *Materials Characterization*, 100:81–87, 2014.

[21] M.P. Ryan, D.E. Williams, R.J. Chater, B.M. Hutton, and D.S. McPhail. Why stainless steel corrodes. *Nature*, 415:770–774, 2002.

[22] Q. Meng, G.S. Frankel, H.O. Colijn, and S.H. Goss. Stainless-steel corrosion and MnS inclusions. *Nature*, 424:389–390, 2003.

[23] S. Dieck, K. Ecke, T. Halle, and P. Rosemann. Improvement of the martensitic stainless steel X46Cr13 by Q&P heat treatment. *IOP Conference Series: Materials Science and Engineering*, 882:012006, 2020.

[24] Z. Zhou, W. Fu, Z. Zhu, B. Li, Z. Shi, and S Sun. Excellent mechanical properties and resistance to cavitation erosion for an ultra-low carbon CrMnN stainless steel through quenching and partitioning treatment. *International Journal of Minerals, Metallurgy, and Materials*, 25 (4):547–553, 2018.

[25] S. Lu, K. Yao, Y. Chen, M. Wang, X. Liu, and X. Ge. The effect of tempering temperature on the microstructure and electrochemical properties of a 13wt.% Cr-type martensitic stainless steel. *Electrochimica Acta*, 165:45–55, 2015.

[26] S. Lu, K. Yao, Y. Chen, M. Wang, Y. Shao, and X. Ge. Effects of austenitizing temperature on the microstructure and electrochemical behavior of a martensitic stainless steel. *Journal of Applied Electrochemistry*, 45 (4):375–383, 2015.

[27] T. Mehner, R. Morgenstern, P. Frint, I. Scharf, M F-X. Wagner, and T Lampke. Corrosion characteristics of a quenching and partitioning steel determined by electrochemical impedance spectroscopy. *IOP Conference Series: Materials Science and Engineering*, 373:012003, 2018.

[28] J. Yang, Y. Lu, Z. Guo, J. Gu, and C. Gu. Corrosion behaviour of a quenched and partitioned medium carbon steel in 3.5 wt.% NaCl solution. *Corrosion Science*, 130:64–75, 2018.

[29] ASTM International. ASTM E407-07. *Standard Practice for Microetching Metals and Alloys*, 2015.

[30] C. Örnek, C. Leygraf, and J. Pan. On the Volta potential measured by SKPFM – fundamental and practical aspects with relevance to corrosion science. *Corrosion Engineering, Science and Technology*, 54 (3):185–198, 2019.

[31] M. Rohwerder and F. Turcu. High-resolution Kelvin probe microscopy in corrosion science: Scanning Kelvin probe force microscopy (SKPFM) versus classical scanning Kelvin probe (SKP). *Electrochimica Acta*, 53 (2):290–299, 2007.

[32] H. Nady, M. El-Rabiei, and M. Samy. Corrosion behavior and electrochemical properties of carbon steel, commercial pure titanium, copper and copper–aluminum–nickel alloy in 3.5% sodium chloride containing sulfide ions. *Egyptian Journal of Petroleum*, 26 (1):79–94, 2017.

[33] C. Abreu, M. Cristobal, R. Losada, X. Novoa, G. Pena, and M. Perez. High frequency impedance spectroscopy study of passive films formed on aisi 316 stainless steel in alkaline medium. *Journal of Electroanalytical Chemistry*, 572 (2):335–345, 2004.

[34] Z. Bou-Saleh, A. Shahryari, and S. Omanovic. Enhancement of corrosion resistance of a biomedical grade 316lvm stainless steel by potentiodynamic cyclic polarization. *Thin Solid Films*, 515 (11):4727–4737, 2007.

[35] J. Rios, J. Calderon, and R. Nogueira. Electrochemical behavior of metals used in drinking water distribution systems: A rotating cylinder electrode's study. *CORROSION*, 69 (9):875–885, 2013.

[36] C.H. Hsu and F. Mansfeld. Technical note: Concerning the conversion of the constant phase element parameter yointo a capacitance. *CORROSION*, 57 (9):747–748, 2001.

[37] S. Salahi, M. Kazemipour, and A. Nasiri. Effects of microstructural evolution on the corrosion properties of AISI 420 martensitic stainless steel during cold rolling process. *Materials Chemistry and Physics*, 258:123916, 2021.

[38] W.T. Yu, J. Li, C.B. Shi, and Q.T. Zhu. Effect of spheroidizing annealing on microstructure and mechanical properties of high-carbon martensitic stainless steel 8Cr13MoV. *Journal of Materials Engineering and Performance*, 26 (2):478–487, 2016.

[39] I. Bösing, G. Marquardt, and J. Thöming. Effect of heat treatment of martensitic stainless steel on passive layer growth kinetics studied by electrochemical impedance spectroscopy in conjunction with the point defect model. *Corrosion and Materials Degradation*, 1 (1):77–91, 2020.

[40] M. Laleh, A. E. Hughes, W. Xu, P. Cizek, and M.Y. Tan. Unanticipated drastic decline in pitting corrosion resistance of additively manufactured 316l stainless steel after high-temperature post-processing. *Corrosion Science*, 165:108412, 2020.

[41] E. McCaffert. *Introduction to Corrosion Science*. Springer, 2009.

[42] R.S. Lillard, M.A. Kashfipour, and W. Niu. Pit propagation at the boundary between manganese sulfide inclusions and austenitic stainless steel 303 and the role of copper. *Journal of The Electrochemical Society*, 163 (8):C440 – C451, 2016.

[43] C. Örnek, M. Liu, J. Pan, Y. Jin, and C. Leygraf. Volta potential evolution of intermetallics in aluminum alloy microstructure under thin aqueous adlayers: A combined dft and experimental study. *Topics in Catalysis*, 61 (9-11):1169 – 1182, 2018.

[44] M. Hayakawa, S. Matsuoka, and K. Tsuzaki. Microstructural analyses of grain boundary carbides of tempered martensite in medium-carbon steel by atomic force microscopy. *MATERIALS TRANSACTIONS*, 61 (9-11):1758 – 1766, 2002.

A

APPENDIX A: FITTING OF EIS DATA

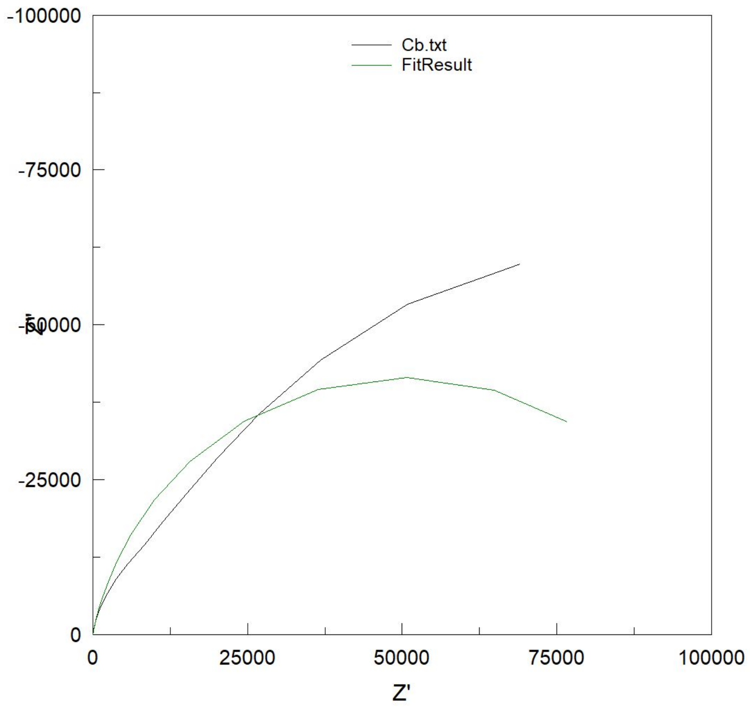

Figure A.1: Fitting of the EIS data using the circuit shown in Figure 4.22a (Nyquist plot)

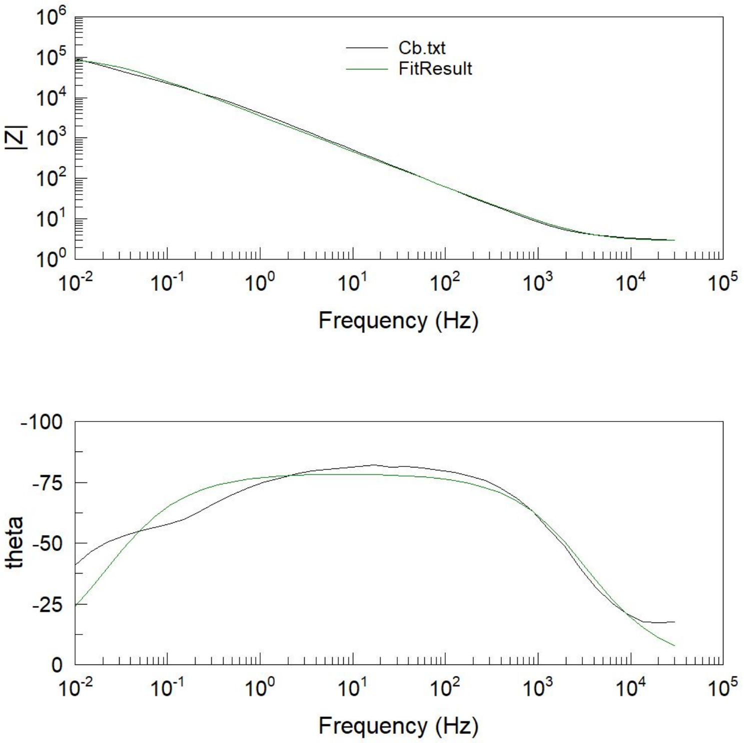

Figure A.2: Fitting of the EIS data using the circuit shown in Figure 4.22a (Bode and phase angle plot)

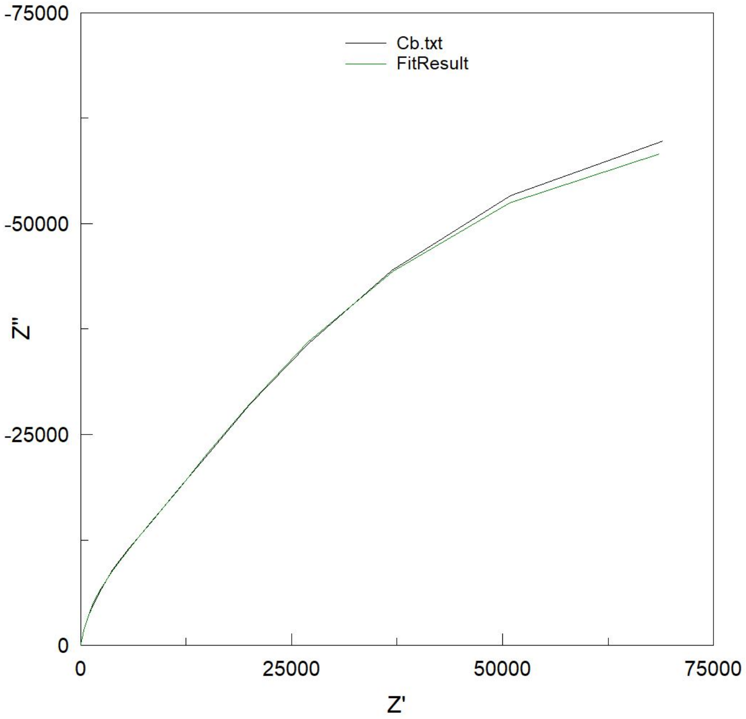

Figure A.3: Fitting of the EIS data using the circuit shown in Figure 4.22b (Nyquist plot)

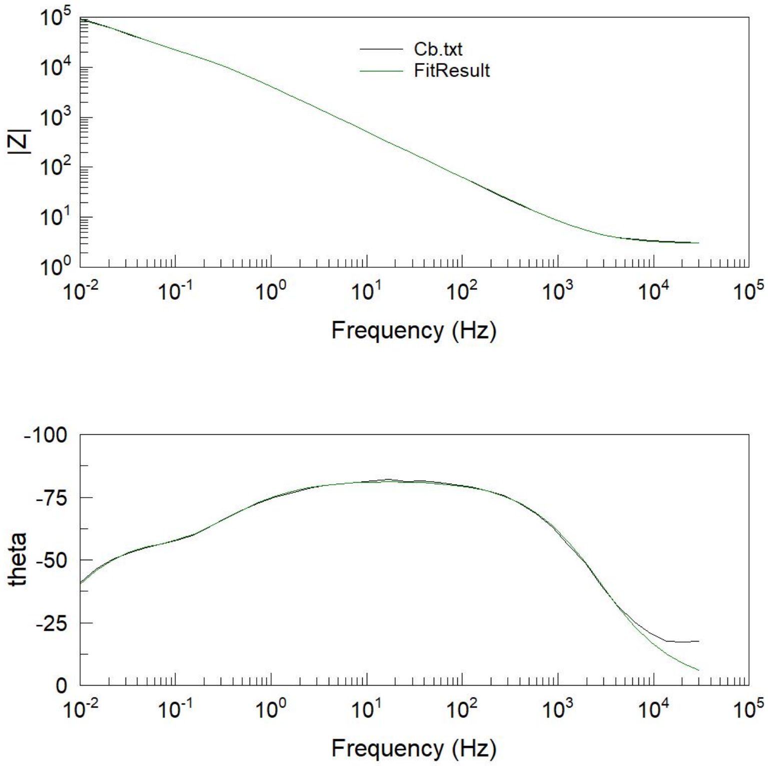

Figure A.4: Fitting of the EIS data using the circuit shown in Figure 4.22b (Bode and phase angle plot)